Spectroscopic and structural properties of synthetic micas on the annite-siderophyllite binary: Synthesis, crystal structure refinement, Mössbauer, and infrared spectroscopy

GÜNTHER J. REDHAMMER,[1,*] ANTON BERAN,[2] JULIUS SCHNEIDER,[3] GEORG AMTHAUER,[4] AND WERNER LOTTERMOSER[4]

[1]Institute of Crystallography, Rheinisch-Westfälische Technische Hochschule Aachen, Jägerstrasse 17/19, D-52056 Aachen, Germany
[2]Institute of Mineralogy and Crystallography, Geocenter, University of Vienna, Althanstrasse 14, A-1090 Vienna, Austria
[3]Institute of Crystallography and Applied Mineralogy, University of Munich, Theresienstrasse 41, D-80333 Munich, Germany
[4]Institute of Mineralogy, University of Salzburg, Hellbrunnerstrasse 34, A-5020 Salzburg, Austria

ABSTRACT

The effect of the incorporation of Al-Tschermak's molecule to the trioctahedral potassium mica annite $\{K\}[Fe_3]<AlSi_3>O_{10}(OH)_2$ on local and average structure has been investigated by hydrothermal synthesis, structure refinement of X-ray powder diffraction data, Mössbauer and infrared spectroscopy. The various types of brackets indicate different structural sites. Samples with compositions $\{K\}[Fe_{3-x}Al_x]<Al_{1+x}Si_{3-x}>O_{10}(OH)_2$ were prepared by hydrothermal techniques. The maximum solubility of Al^{3+} is limited to $x = 0.92$ at 500 °C and to $x = 0.82$ at 700 °C. The main factor controlling the substitution limits is the ditrigonal distortion of the tetrahedral rings. Lattice parameters decrease linearly with increasing Al^{3+} content of the mica. A considerable decrease of M2-O and nearly no change of M1-O bond lengths with increasing Al^{3+} contents is indicative of preferred occupation of the M2 site by $[Al^{3+}]$. Changes in K-O distances are also very pronounced and reflect the ditrigonal distortion of the tetrahedral sheet. The bimodal ferrous quadrupole splitting distribution (QSD) in annite, extracted from Mössbauer spectra, becomes narrower and more centered around 2.60 mm/s with increasing Al^{3+} contents, and its evolution suggests an increasing deviation from ideal octahedral coordination of Fe by O, illustrated by the increasing octahedral flattening angle ψ. The population of individual QSD components proves that it is impossible to resolve cis and trans M-sites in micas by Mössbauer spectroscopy. In the hydroxyl stretching region, up to 7 bands are observed in the infra-red spectra which correspond to OH groups adjacent to 3 Fe^{2+} (N-bands), to OH groups coordinated by Fe^{2+}, Al^{3+}, and Fe^{3+} (I-bands) and to configurations having one octahedral vacancy (V-bands). N- and I-type bands are shifted toward lower wavenumbers with increasing Al^{3+} content because of increasing $OH\cdots O_{tet}$ interactions.

INTRODUCTION

Annite, $\{K\}[Fe_3]<AlSi_3>O_{10}(OH)_2$, with { }, [ ] and < > representing K in the interlayer site, Fe in the octahedral and one Al and three Si in tetrahedral sites respectively, is the theoretical iron end-member of the trioctahedral biotite mica series, an important rock forming mineral group. Biotite, $\{K\}[(Fe^{2+},Mg)_3]<AlSi_3>O_{10}(OH)_2$ shows atomic substitutions mainly of Mg by Fe^{2+}, however, natural samples also contain substantial amounts of Al^{3+} in octahedral coordination. The name siderophyllite is used for the theoretical aluminium end-member $\{K\}[Fe_2^{2+}Al^{3+}]<Al_2^{3+}Si_2>O_{10}(OH)_2$. Incorporation of Al^{3+} into annite is accomplished via the coupled substitution $^{[6]}Fe^{2+}$ + $^{[4]}Si^{4+} \leftrightarrow$ $^{[6]}Al^{3+}$ + $^{[4]}Al^{3+}$ (Al-Tschermak's substitution). However, various other cations such as Li^+, Ni^{2+}, Co^{2+}, Zn^{2+}, Cu^{2+}, Mn^{2+}, Mn^{3+}, Fe^{3+} and Ti^{4+} can enter the octahedral sites [ ], Na^+, Rb^+ can partly replace K^+ in the interlayer site { }, and Fe^{3+},

Al^{3+}, Ga^{3+} and Ge^{4+} can enter the tetrahedral site < >. To understand the complex crystal chemistry and the effect of these various possible substitutions on stability, global and local structure and cationic environments, the "simplified" solid solutions series between the two main end-member compositions annite (ann) and siderophyllite (sid) was studied. We describe syntheses, stability, and structure refinements of X-ray powder patterns of the title compounds and compositions along the ann-sid binary to investigate possible cationic ordering of Fe^{2+} and Al^{3+} on the octahedral sites. Mössbauer and infrared spectroscopy were used to address changes in the local and electronic environments of the cations-mainly on the octahedral sites. The Mössbauer results demonstrate that the two different octahedral M sites in the mica structure are impossible to resolve by this method.

The structure of trioctahedral micas is built up by a negatively charged 2:1 composite layer. Two tetrahedral sheets with the apices pointing together, sandwich one octahedral sheet. Charge balance is achieved by the large interlayer cations. The structures of annite and phlogopite were described in detail by

---

Hazen and Burnham (1973), but except for the numerous investigations on natural biotites (e.g., Brigatti and Davoli 1990; Brigatti et al. 1991), there is a lack of structural information for the very Fe rich and Fe-Al rich biotites, and no systematic study does exist so far regarding the changes of structural parameters as a function of progressive Al-Tschermak's substitution in annite.

Syntheses of annite were reported by Mercier et al. (1996), Redhammer et al. (1993), Dachs (1994) and references in these papers, the substitution of aluminum in annite by Rutherford (1973) and Hewitt and Wones (1975), who both found the substitution to be limited to about 0.8 apfu (atoms per formula unit) on the octahedral sites. In contrast, Levillain et al. (1981) report the synthesis of a siderophyllite with approximately ideal composition. Benisek et al. (1996) and Benisek et al. (1999) investigated the activity-composition relationship and the heat capacities of Tschermak's substituted Fe-biotites.

Mössbauer spectroscopy has used to define valence state and coordination of iron in natural and synthetic (e.g., Annersten 1974; Levillain et al. 1981; Dyar and Burns 1986; Dyar 1990 and references therein). Mössbauer spectroscopy also has high potential to characterize the local electronic and geometric environment around the iron atom and to record changes in polyhedral distortion (e.g., deviations from ideal octahedral coordination) as a function of chemical composition (e.g., Rancourt et al. 1994a, 1996; Redhammer 1998).

The approach to refine Mössbauer spectra of mica with Lorentzian shaped doublets and applying different kinds of constraints to extract M2/M1 site occupation ratios (e.g., Annersten 1974; Dyar and Burns 1986; Dyar 1990; Redhammer et al. 1993, 1995) was critically discussed by Rancourt et al. (1994a, 1994b) and Rancourt (1994a, 1994b). To fit the spectral resonance absorption contributions of micas, a Voigt based quadrupole-splitting distribution (QSD) method (Rancourt and Ping 1991; Ping et al. 1991) was introduced. The application of the QSD method to characterize synthetic trioctahedral micas is outlined in detail by Rancourt et al. (1994a) for the annite-phlogopite join, by Rancourt et al. (1996) for (OH)-F annites and by Redhammer (1998) for micas with various octahedral and tetrahedral substitutions.

Natural and synthetic micas have been investigated by infrared spectroscopy with emphasis on the OH regions (Farmer 1974; Jenkins 1989; Boukili 1996; Benisek et al. 1999). Robert and Kodama (1988) generalized the correlation between hydroxyl-stretching wavenumbers and compositions of synthetic di- and trioctahedral Mg-Al micas. Some discussions on the OH-stretching region of annite is also found in Redhammer et al. (1993) and in Rancourt et al. (1994b), however, substantial discrepancies do exist concerning band assignment, especially in annite.

EXPERIMENTAL METHODS

All syntheses were performed by conventional hydrothermal techniques (cold sealed pressure vessels). For details see Redhammer et al. (1993) and Dachs (1994) and Table 1.

Starting materials for syntheses were stoichiometric gels $\{K\}[Fe_{3-x}Al_{3+x}]<Al_{1+x}Si_{3-x}>O_{10}(OH)_2$, $0 \leq x \leq 1.0$. The gels were prepared according to the method of Hamilton and Henderson (1968) using K_2CO_3, $Fe(NO_3)_3*9H_2O$, $Al(NO_3)_3*9H_2O$ and $(C_2H_5O)_4Si$ (all Merck, at least 99%) as sources for K, Fe, Al and Si respectively. All ferric iron present in the gels was transformed to the divalent state by reducing it in a H_2 stream at 600 °C for at least 4 hours. Some experiments were also conducted using stoichiometric mixtures of the oxides Fe_2O_3, Al_2O_3, SiO_2, and K_2CO_3 as starting materials. Redox conditions were fixed using solid state oxygen buffers and the tube-in-tube technique. The starting materials together with ~15 wt% distilled H_2O were sealed into Ag/Pd tubes and placed into larger Au tubes, together with the appropriate solid state buffer and ~15 wt% distilled H_2O.

The chemical composition of selected samples was determined using an electron microprobe (Jeol JXA 8600, automated by LEMAS system, acceleration voltage 15 kV, initial beam current 30 nA, beam focused to 1 μm). The following silicates and oxides were used as a standards: sanidine (K), pure iron (Fe), quartz (Si), and corundum (Al). Mica products were pressed to flat disks, fixed onto glass slides with "liquid carbon," covered with carbon and analyzed.

For qualitative phase analysis and lattice parameter determination, step scan powder diffraction data were collected with a Siemens D-500 Bragg-Brentano powder diffractometer system equipped with a secondary graphite monochromator. Samples were smeared onto zero-background single-crystal silicon plates, 20 mm in diameter, and rotated during measurements. Profiles were taken between 5 and 85° 2θ using a step interval of 0.02° 2θ and a step counting time of 15 s. Pure synthetic silicon (a = 5.43088 Å) was added as internal standard.

For structure refinements the powder diffraction experiments were performed on a focusing STOE-STADIP diffractometer equipped with a curved Ge(111) monochromator to produce strictly monochromatic Mo$K\alpha_1$ radiation. To avoid orientation effects of the sample crystallites, the mica powders were inserted into 0.3 mm-diameter glass capillaries which were rotated during measurement. The data collection used an overlapping step-scan mode of a linear position-sensitive detector of about 5° acceptance angle and 0.02° channel width, yielding 2500 data points in the 2θ range from 2° to 52°. Each scan was repeated 10 times to monitor the stability of the diffractometer, and the scans were then summed up for better averaging.

Lattice parameters were extracted by full-pattern profile refinements using the program "fullprof" (Rodriguez-Carvajal 1996); the structure refinements by the Rietveld method were also done with "fullprof." The pseudo-Voigt function was used to simulate the peak shape, intensities within six times of the FWHM (full width at half maximum) were assumed to contribute to one reflection. The angular dependence of the peak FWHM was refined with three free parameters using the formula of Cagliotti et al. (1958) and peaks below 45° 2θ (Cu-case) and 25° 2θ (Mo case) were corrected for asymmetry according to Rietveld (1969). Backgrounds were fixed manually. Peaks below 20° 2θ (Cu-case) were excluded from profile and structure refinements because of large peak asymmetry. All micas were refined in $C2/m$ (No. 12) space group (1M polytype). Initial structure parameters were taken from the single-crystal refinement of annite given by Hazen and

Burnham (1973). During the X-ray powder data refinements, the Al/Si ratio in tetrahedral sites was constrained to the data found by EMP analysis. Al and Fe were allowed to vary over the M sites during refinements constraining the total $[Al^{3+}]$ content to the data found by EMP analysis. Isotropic atomic displacement parameters were released in a final refinement cycle and gave reasonable values. Correlations with the occupancy of Fe^{2+} and Al^{3+} on the M sites were below 20% in each case.

Transition ^{57}Fe Mössbauer spectra were recorded at 293 K using a conventional Mössbauer apparatus in horizontal arrangement (Halder Electronic GmbH, Germany) using a $^{57}Co/Rh$ single line thin source with initial activity of 60 mCi. The spectrometer was operated in constant acceleration mode with a symmetric triangular velocity shape and a multi-channel analyser with 1024 channels. The velocity range was ±4 mm/s and the velocity was frequently calibrated to a thin α-Fe foil. The isomer shift δ is given relative to α-Fe in this work. Absorbers were prepared to have a nominal density of 5 mg Fe per square cm. The appropriate amount of the mica sample was suspended in powder sugar to obtain a random distribution and finally filled into Cu-rings, 10 mm inner diameter and 2 mm in depth. The two symmetric spectra (512 channels each) obtained were folded, calibrated to α-iron and evaluated by the Voigt based QSD method (Rancourt and Ping 1991; Ping et al. 1991; Rancourt et al. 1994a; Rancourt et al. 1996) with the program RECOIL. This method uses a certain number m of generalized sites each having its own continuous QSD, built up by a certain number of n Gaussian components. All the spectra of this study were corrected for thickness effects assuming a representative average recoilless fraction of $f = 0.7$. Γ was constrained to 0.198 mm/s for all generalized sites.

IR spectra were collected on a Perkin Elmer FTIR spectrometer 1760X, equipped with a ceramic light source, a DTGS detector, and a CsI microfocus accessory. The initially dried finely powdered samples were prepared as KBr-microdisks and/or mixed with a few drops of "poly-oil" (polychlorotrifluorethylene) and smeared between two NaCl plates. KBr-microdisks were dried at 110 °C for 12 hours. Background and sample spectra were obtained from 36 scans each from 1400 cm^{-1} to 400 cm^{-1} and from 4000 to 3000 cm^{-1} with a resolution of 4 cm^{-1}. Data were processed with the IRDM software (Perkin Elmer). For annite we recorded spectra both from KBr-microdisks and from samples prepared with "poly-oil." The later method would favor preferred orientation of mica flakes, however, we did not observe any difference between the two preparation methods. Furthermore, tilting KBr-micro-disks by 15° did not change the appearance of the spectrum. Thus we conclude that our spectra are not affected by preferred orientation effects.

Spectra fitting was done with the program PeakFit, version 4 for win32 (Jandel Scientific Software). The spectroscopic peak-fit function "Gaussian-Lorentzian Sum" was used to mathematically describe the peak shape with:

$$y = 2a_0 \left[\frac{a_3 \sqrt{\ln 2}}{a_2 \sqrt{\pi}} exp\left(-4\ln 2 \left(\frac{x - a_1}{a_2} \right)^2 \right) + \frac{1 - a_3}{\pi a_2 \left[1 + 4\left(\frac{x - a_1}{a_2} \right)^2 \right]} \right]$$

and a_0 = area, a_1 = center of the peak, a_2 = width of the peak, a_3 = shape of the peak. Only peaks were fitted, which at least appeared as visible shoulders in the raw spectrum. The peak shape parameter a_3 was 1 or very close to 1 in all cases, i.e., showed the refined peaks having symmetric Gaussian shape. Papin et al. (1997) also found the measured absorption bands to be Gaussian in shape in synthetic phlogopite. During fitting process, different sets of starting parameters were tested giving almost identical results.

RESULTS

Syntheses of micas

The stability of annite is mainly a function of temperature and redox conditions and is rather restricted within the T-log f_{O_2} field (e.g., Dachs 1994; Cyang et al. 1996 and references in both papers). At 4 kbar and temperatures $T \leq 700$ °C annite is the stable phase at the conditions of the QMF (quartz+magnetite/fayalite) and more reducing solid state buffers. Table 1[1] compiles the results of selected syntheses experiments including some new experiments to crystallize annite.

In general it was possible to synthesize high quality mica products along the annite-siderophyllite solid solution series. All experiments, performed with the MW solid state buffer at different temperatures yield single phase samples for $0.12 \leq x \leq 0.75$. For the $x = 0.87$ composition, pure products were obtained at 500 °C, whereas traces of kalsilite ($KAlSiO_4$) and corundum (α-Al_2O_3) appeared at 700 °C. For $x = 1.0$, it was not possible to synthesize single phase products, corundum appeared at each temperature used. For compositions with $0.12 \leq x \leq 0.25$ and NNO conditions synthesis experiments showed single phase products at 500 °C, 600 °C, and 650 °C, very rare traces of magnetite (Fe_3O_4) + leucite ($KAlSi_2O_6$) + sanidine ($KAlSi_3O_8$) appeared as additional phases at 700 °C, and magnetite + leucite were found in clearly detectable amounts throughout the solid solution series at 780 °C. Corundum appeared for $x = 0.87$ above 600 °C and was always present for $x = 1.0$.

The micas, synthesized from gels, appear as fine grained powders, displaying a dark olive-green color, which becomes pale blue-green with increasing Al content. Figure 1a shows a scanning electron microscopy (SEM) image of no. A61, which is typical for annites, synthesized from gels. Mica flakes are rather uniform in size and not larger than 1 mm in diameter. A SEM image of annite, grown from an oxide mixture (no. an/co/no. 1) is shown in Figure 1b. An increase of crystal size is evident; individual flakes are up to 4 mm thick with diameters up to 15 mm. Compared to experiments using gels as starting material, oxide mixtures produce much larger crystals in shorter times.

Mineral chemistry

The structural formulae of selected micas, derived from microprobe analysis, are in Table 2. The actual composition of the micas generally agrees with the stoichiometry of the start-

TABLE 1. Run conditions and experimental results of annite-siderophyllite syntheses

Run	Start*	T (°C)	P (bar)	t (h)	Buffer†	Product‡
A44	gel	650	4000	980	MW	ann
A61	gel	650	4000	689	MW	ann (fa)
A62	A61	600	4000	92	NNO	ann
A63	A61	500	4000	92	HM	ann, he, sa
A64	A61	650	4000	57	HM	he, mt, sa, ann
ann/CO/no. 1	oxid	650	4000	622	MW	ann
sid12/no. 1	gel	700	4000	911	NNO	mi
sid12/no. 2	gel	600	4000	1128	NNO	mi
sid12/no. 3	gel	500	4000	787	NNO	mi
sid12/no. 4/650	gel	650	4000	1128	NNO	mi
sid12/no. 10/650	sid12/no. 4	650	4000	273	MW	mi
sid25/no. 1	gel	600	4000	1058	NNO	mi
sid25/no. 2	gel	700	4000	991	NNO	mi
sid25/no. 3	gel	780	1500	1269	NNO	mi,(lc, mt)
sid25/no. 4	gel	650	4000	780	NNO	mi
sid25/no. 10	sid25/no. 4	650	4000	243	MW	mi
sid37/no. 1	gel	700	4000	901	NNO	mi
sid37/no. 2	gel	600	4000	1128	NNO	mi
sid37/no. 10	sid37/no. 4	650	4000	243	MW	mi
sid50/no. 1	gel	600	4000	1058	NNO	mi
sid50/no. 2	gel	700	4000	991	NNO	mi
sid50/no. 10	sid50/no. 4	650	4000	243	MW	mi
sid62/no. 1	gel	700	4000	911	NNO	mi
sid62/no. 2	gel	600	4000	1128	NNO	mi
sid62/no. 10	sid62/no. 4	650	4000	237	MW	mi
sid75/1	gel	600	4000	1058	NNO	mi
sid75/2	gel	700	4000	991	NNO	mi
sid75/no. 10	sid75/no. 4	650	4000	237	MW	mi
sid87/no. 1	gel	700	4000	911	NNO	mi
sid87/no. 2	gel	600	4000	1128	NNO	mi
sid87/no. 10	sid87/no. 4	650	4000	622	MW	mi
sid100/1	gel	600	4000	1058	NNO	mi, (co)
sid100/2	gel	700	4000	991	NNO	mi, (co)
sid100/3	gel	780	1500	1149	NNO	mi, (lc)
sid100/4	gel	650	4000	750	NNO	mi, (ks, co)
sid100/5	gel	500	4000	750	NNO	mi, (co)
sid100/no. 10	sid100/no. 4	650	4000	237	MW	mi, (co)

Notes: Temperatures are accurate to ± 3 °C, pressure constancy was ± 200 bars. Pure water was used as a pressure medium.
* gel = gel used as starting material, oxid = oxid mixture used as starting material. Run names with sid12 have × = 0.12, sid25 × = 0.25, sid37 × = 0.37, sid50 × = 0.50, sid62 × = 0.62, sid75 × = 0.75, sid87 × = 0.87, sid100 × = 1.00.
† Solid state buffer mixtures: MW = magnetite/ wuestite, NNO = nickel/ nickeloxide.
‡ ann = annite, mi = mica (ann - sid binary), mt = magnetite, ks = kalsilite, lc = leucite, co = corundum, fa = fayalite, he = hematite.

TABLE 2. Stoichiometric coefficients of selected synthetic micas of the annite-siderophyllite join

sample	{K$^+$}	[Fe^{2+}]	[Fe^{3+}]	[Al^{3+}]	<Si^{4+}>	<Al^{3+}>
sid12/no. 1/600	1.00(1)	2.76(2)	0.11	0.13(1)	2.87(1)	1.13(1)
sid12/no. 2/700	1.00(1)	2.51(2)	0.33	0.17(2)	2.87(2)	1.13(2)
sid12/no. 10/650	1.00(1)	2.80(4)	0.08	0.11(2)	2.85(2)	1.15(2)
sid25/no. 1/600	1.00(1)	2.52(2)	0.19	0.26(1)	2.80(3)	1.20(1)
sid25/no. 2/700	1.00(1)	2.63(2)	0.11	0.25(1)	2.78(1)	1.22(1)
sid25/no. 10/650	1.00(2)	2.62(5)	0.08	0.26(3)	2.80(2)	1.20(2)
sid37/no. 1/700	1.01(1)	2.43(5)	0.13	0.40(3)	2.68(2)	1.32(3)
sid37/no. 2/600	1.01(1)	2.38(4)	0.21	0.38(2)	2.67(1)	1.33(2)
sid37/no. 10/650	1.02(3)	2.62(3)	0.04	0.33(2)	2.66(2)	1.34(2)
sid50/no. 2/700	1.02(1)	2.41(2)	0.05	0.50(1)	2.57(1)	1.43(1)
sid50/no. 10/650	1.01(2)	2.43(4)	0	0.51(2)	2.59(1)	1.41(2)
sid62/no. 1/700	1.03(1)	2.33(4)	0	0.62(4)	2.42(4)	1.58(4)
sid62/no. 2/600	1.02(1)	2.23(4)	0.13	0.67(2)	2.47(2)	1.53(2)
sid62/no. 10/650	1.02(2)	2.37(3)	0	0.60(4)	2.43(3)	1.57(4)
sid75/no. 1/600	1.00(2)	2.15(5)	0.08	0.75(2)	2.31(4)	1.69(2)
sid75/no. 2/700	1.01(3)	2.22(6)	0	0.75(4)	2.28(4)	1.72(4)
sid75/no. 10/650	1.02(2)	2.18(3)	0	0.75(3)	2.32(3)	1.68(3)
sid87/no. 1/700	1.03(3)	2.14(4)	0	0.78(1)	2.26(2)	1.74(1)
sid87/no. 2/600	1.00(2)	2.14(4)	0	0.84(5)	2.26(3)	1.74(5)
sid87/no. 10/650	1.00(2)	2.17(5)	0	0.78(2)	2.28(3)	1.72(2)
sid100/no. 1/600	1.00(3)	2.06(4)	0	0.86(4)	2.18(3)	1.82(4)
sid100/no. 2/700	1.02(2)	2.16(3)	0.06	0.78(5)	2.17(3)	1.83(5)
sid100/no. 5/500	1.01(2)	2.04(3)	0	0.92(3)	2.08(4)	1.92(2)
sid100/no. 10/650	1.00(2)	2.15(3)	0	0.82(2)	2.19(3)	1.81(2)

Note: Derived from microprobe analyses and Mössbauer spectroscopy, numbers in parentheses give one standard deviation.
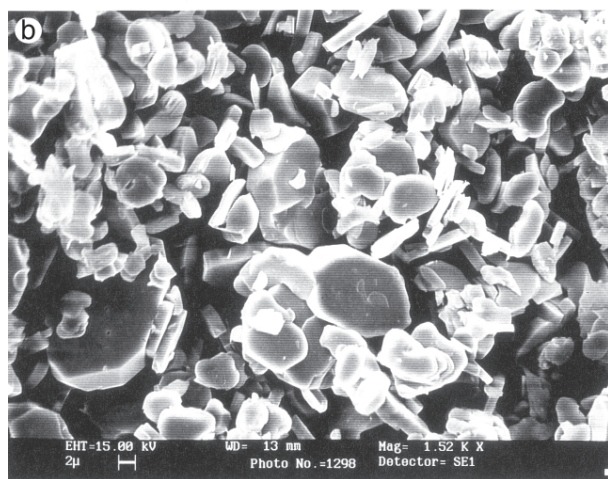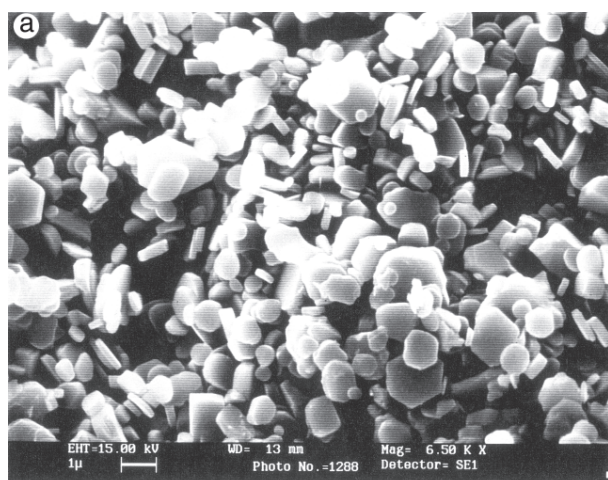
FIGURE 1. Scanning electron microscopy images of synthetic annite: (**a**) synthesized from gel starting material at 700 °C, (**b**) synthesized from oxide mixture at 700 °C.

FIGURE 2. Mineral chemistry of synthetic micas $K[Fe_{3-x}Al_x]$ $<Al_{1+x}Si_{3-x}>O_{10}(OH)_2$ on the ann-sid binary: limitation of Al^{3+} solubility as a function of synthesis temperature.

ing materials. In terms of the $[Fe^{2+}]$ to $[Al^{3+}]$ concentrations on the octahedral sites, the data for the synthetic micas fall close to the theoretical ann-sid-join. There is a slight tendency to a small deficiency of aluminum in the Al^{3+}-enriched samples. In a plot of the content of $[Al^{3+}]$ vs. the $<Al^{3+}>$ content, the data points are not exactly on the theoretical ann-sid join but are shifted slightly toward higher $[Al^{3+}]$ concentrations. These samples tend to have octahedral vacancies. Mineral chemistry distinctly exhibits the limited substitution of Al in annite. Microprobe analyses of the micas having starting compositions with $x = 0.87$ and $x = 1.00$ further show, that the maximum concentration of $[Al^{3+}]$ on the octahedral sites is temperature dependent (Fig. 2). For starting materials with $x = 1.00$, the maximum solubility of Al in annite was 0.92 apfu (atom per formula unit) $[Al^{3+}]$ at 500 °C, but only 0.78 apfu $[Al^{3+}]$ at 700 °C. Similar results observed for $x = 0.87$, where 0.84 apfu $[Al^{3+}]$ were found at 600 °C, but only 0.78 apfu $[Al^{3+}]$ at 700 °C (Table 2).
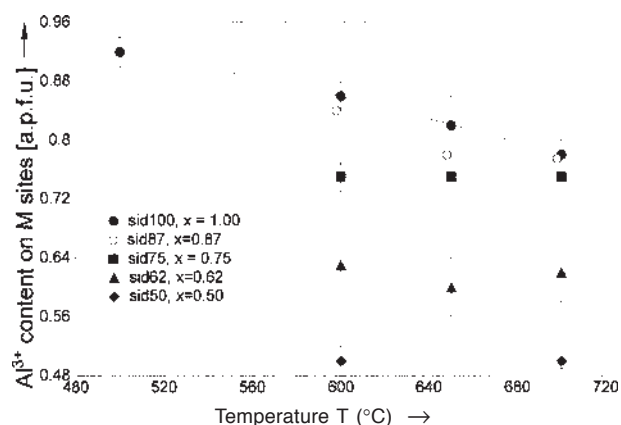
Lattice parameters and structure refinements

The XRPD data collection, details on structure refinements, and unit-cell dimensions for selected ann-sid micas are in Table 3, final atomic positions and atomic displacement parameters are in Table 4, and selected interatomic distances are in Table 5. In the present Rietveld refinements the agreement between observed and calculated data is good. This is expressed by the various agreement factors, e.g., the Bragg reliability factor R_B ranging between 3.4 and 4.6.

Lattice parameters. Variations of lattice parameters of the synthetic micas (Fig. 3) are in agreement with data from Hewitt and Wones (1975) and Benisek et al. (1999). The lattice parameters are a function of Al^{3+} content and show isotropic variations for the a and b edge lengths. The *a*, *b*, and *c* unit-cell parameters decrease distinctly by ~0.03 Å, ~0.055 Å, and 0.04 Å, respectively, from ann to sid, however, the compositional dependence of the monoclinic angle β is small and exhibits a discontinuity at ~2.4 apfu Al^{3+}_{tot}. The *c* cell edge length behaves similarly.

Site occupation. The Rietveld method provides accurate site occupations if reasonable starting values for the isotropic atomic displacement parameters (B_{iso}) are used (Della Ventura et al. 1993). For the M sites the occupation factors were restrained as follows: Al + Fe = 0.25 and 0.50 for M1 and M2, respectively. Several starting models were used in refining the Fe-Al distribution on the M-sites. Refinements, however, always converged to the data (Table 6) as graphically displayed in Figure 4d. Al is equally distributed over the two M sites in the Al-poor micas. With increasing Al content a pronounced preference of Al^{3+} for the M2 site is detected. The $[Al^{3+}]$ content does not exceed 0.14 apfu on the M1 site and remains rather constant above $x \sim 0.5$.

In the final refinement cycles, the isotropic atomic displacement parameters B_{iso} were also refined. The tetrahedral and the M1 atoms have the lowest values and potassium on the interlayer site the highest one. The basal oxygen atoms O1 and O2 tend to have slightly higher isotropic thermal parameters than O3 and O4.
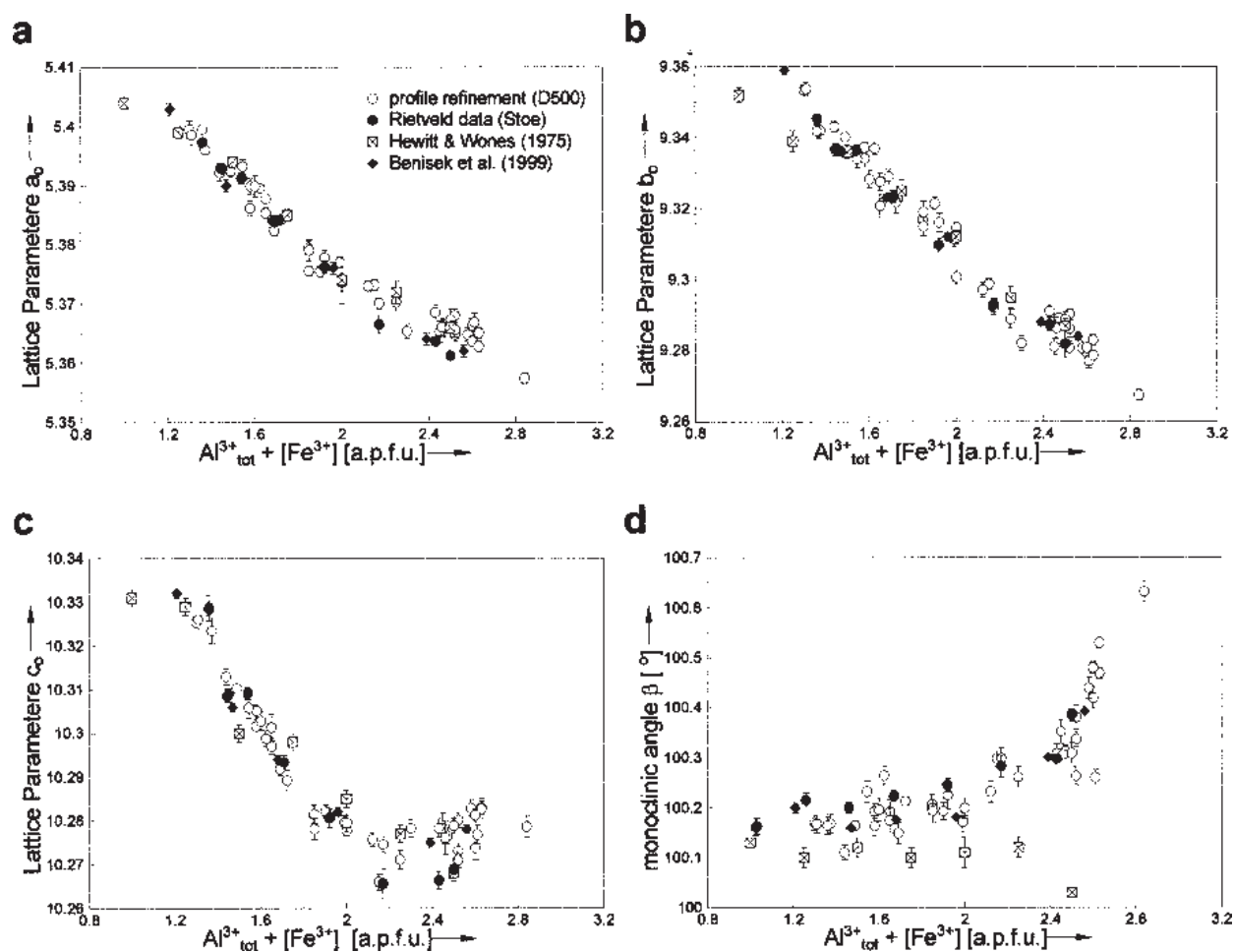
FIGURE 3. Variation of lattice parameters of synthetic micas on the ann-sid binary as determined by Rietveld refinements (filled circles, λ = Mo$K\alpha_1$ radiation) or full pattern refinement (open circles, λ = Cu$K\alpha_{1,2}$ radiation) of X-ray powder diffraction data. Lattice parameters of Hewitt and Wones (1975) are also included (filled triangles).

TABLE 3. Data collection and structure refinement details for selected synthetic annite-siderophyllite samples

	A44	sd12 no. 10	sd25 no. 10	sd37 no. 10	sd50 no. 10	sd62 no. 10	sd75 no. 10	sd87 no. 10
R_p	10.8	7.24	10.0	9.54	10.6	11.0	9.48	10.5
R_{wp}	9.54	7.87	8.63	9.39	10.4	10.3	9.62	10.0
R_B	4.18	2.32	3.42	3.44	4.13	4.59	3.96	4.57
D_W d-statistics	1.679	1.574	1.715	1.620	1.564	1.694	1.582	1.561
U	0.151(13)	0.19(1)	0.124(10)	0.155(14)	0.163(19)	0.221(28)	0.19(2)	0.27(3)
V	−0.071(6)	−0.07(2)	−0.055(5)	−0.062(6)	−0.070(7)	−0.088(10)	−0.073(7)	−0.076(11)
W	0.0193(7)	0.0191(7)	0.0153(5)	0.0174(6)	0.0198(8)	0.0256(9)	0.0198(7)	0.0212(10)
γ_1	0.75(2)	0.64(3)	0.78(2)	0.61(2)	0.59(3)	0.26(3)	0.53(2)	0.49(2)
γ_2	−0.003(1)	−0.001(1)	−0.005(1)	0.001(1)	0.006(1)	0.013(1)	0.002(1)	0.001(1)
Preferred orientation	1.021(2)	1.035(2)	1.026(2)	1.036(2)	1.031(2)	1.017(2)	1.014(2)	1.021(2)
a_o	5.3899(8)	5.3944(6)	5.3883(6)	5.3812(7)	5.3732(8)	5.3635(15)	5.3607(7)	5.3582(10)
b_o	9.3367(11)	9.3454(10)	9.3365(9)	9.3234(11)	9.3097(14)	9.2929(24)	9.2874(12)	9.2819(16)
c_o	10.3086(10)	10.3284(10)	10.3092(8)	10.2934(10)	10.2807(13)	10.2837(22)	10.2664(12)	10.2688(17)
β	100.16(1)	100.22(1)	100.20(1)	100.22(1)	100.24(1)	100.28(1)	100.30(1)	100.39(1)

Note: R parameters according to Rietveld (1967) and Hill and Fischer (1990).

TABLE 4. Atomic fractional coordinates and isotropic atomic displacement parameters for the synthetic annite-siderophyllite micas

		A44	sd12no.10	sd25no.10	sd37no.10	sd50no.10	sd62no.10	sd75no.10	sd87no.10	G-117*
T	x	0.5746(24)	0.5714(20)	0.5729(16)	0.5724(17)	0.5720(20)	0.5748(16)	0.5740(14)	0.5741(16)	0.5754(2)
	y	0.1664(12)	0.1668(11)	0.1663(9)	0.1667(8)	0.1670(11)	0.1674(11)	0.1665(8)	0.1673(9)	0.16681(7)
	z	0.2254(5)	0.2258(5)	0.2263(3)	0.2260(4)	0.2261(4)	0.2269(5)	0.2266(4)	0.2271(5)	0.22579(8)
	B_{iso}†	1.07(12)	0.6(1)	0.89(10)	0.77(10)	0.69(12)	0.99(11))	0.68(6)	0.73(11)	0.99(2)
M1	B_{iso}	0.9(2)	0.7(2)	0.5(1)	0.7(2)	0.5(2)	0.9(2)	0.8(1)	0.7(1)	0.87(2)
M2	y	0.8333(7)	0.8333(7)	0.8316(6)	0.8323(6)	0.8318(6)	0.8327(7)	0.8319(6)	0.8327(4)	0.83196(6)
	B_{iso}	1.60(15)	0.97(14)	0.91(12)	0.97(12)	1.08(15)	1.1(1)	0.95(9)	1.0(1)	0.89(2)
K	B_{iso}	3.8(3)	4.0(3)	3.7(2)	2.8(2)	2.1(3)	2.4(2)	1.9(1)	2.0(1)	2.85(5)
O1	x	0.8138(40)	0.8085(32)	0.8158(30)	0.8201(31)	0.8251(37)	0.8290(56)	0.8333(30)	0.8343(32)	0.8260(4)
	y	0.2410(14)	0.2466(13)	0.2361(10)	0.2308(11)	0.2255(13)	0.2237(12)	0.2205(11)	0.2190(12)	0.2298(3)
	z	0.1777(14)	0.1744(7)	0.1752(11)	0.1758(11)	0.1759(13)	0.1770(13)	0.1768(11)	0.1766(12)	0.1695(2)
	B_{iso}	3.2(4)	2.5(2)	2.4(2)	2.3(2)	1.8(2)	2.0(2)	2.1(2)	2.0(2)	2.01(4)
O2	x	0.5457(28)	0.5417(26)	0.5342(24)	0.5277(24)	0.5216(28)	0.5117(29)	0.5069(26)	0.5020(25)	0.5158(6)
	z	0.1676(21)	0.1722(20)	0.1701(17)	0.1700(16)	0.1711(20)	0.1734(19)	0.1740(16)	0.1748(18)	0.1706(3)
	B_{iso}	2.4(6)	0.9(3)	1.6(3)	1.2(2)	1.6(3)	1.9(3)	1.8(3)	2.2(2)	1.93(6)
O3	x	0.6373(26)	0.6365(20)	0.6369(34)	0.6368(34)	0.6370(30)	0.6391(34)	0.6384(31)	0.6385(31)	0.6319(5)
	y	0.1675(17)	0.1665(17)	0.1670(13)	0.1678(13)	0.1690(19)	0.1689(16)	0.1697(13)	0.1700(14)	0.1679(2)
	z	0.3939(11)	0.3940(11)	0.3933(9)	0.3933(10)	0.3943(13)	0.3950(12)	0.3945(11)	0.3958(11)	0.3918(2)
	B_{iso}	1.5(2)	0.9(1)	1.2(1)	1.2(1)	1.3(1)	2.0(2)	1.9(1)	1.9(3)	1.44(4)
O4	x	0.1367(32)	0.1323(54)	0.1309(44)	0.1329(42)	0.1332(48)	0.1310(36)	0.1309(40)	0.1289(40)	0.1271(6)
	z	0.3860(17)	0.3877(17)	0.3882(14)	0.3909(14)	0.3924(15)	0.3926(16)	0.3928(14)	0.3928(15)	0.3963(3)
	B_{iso}	1.9(4)	1.4(2)	1.5(2)	1.1(2)	1.6(3)	1.6(2)	1.4(2)	1.4(2)	1.61(5)

Notes: Determined by the Rietveld method, including single-crystal data for a natural Al-Fe rich biotite G-117*. Special positions for following atoms: M1 = 0, 0.5, 0.5; M2 = 0, y, 0.5; K = 0, 0, 0; O2 = x, 0, z; O4 = x, 0, z.
* Single crystal structural refinement of natural biotite Litchfield/Barker biotite G-117 (Redhammer and Roth, 1998, unpublished results, Stoe imaging plate diffractometer measurement, Mo $K\alpha$ radiation: 640 independent reflections, S.G. $C2/m$, $Z = 2$, lattice parameters: $a = 5.377(1)$ Å, $b = 9.308(2)$ Å, $c = 10.283(2)$ Å, $\beta = 100.22(2)°$; $R_{int} = 0.029$, R_1 (all data) = 0.0448, wR_2 (all data) = 0.053; chemical analysis performed by Darby M Dyar: $\{K_{0.99}Na_{0.01}\}[Fe^{2+}_{1.90}Fe^{3+}_{0.48}Al_{0.27}Mg_{0.11}Mn_{0.03}Ti_{0.04}]<Si_{2.55}Al_{0.45}>O_{10}(OH_{1.79}F_{0.07}Cl_{0.02})$.
† B_{iso} = isotropic atomic displacement parameter.

TABLE 5. Selected interatomic distances (in angstroms) for synthetic micas on the annite-siderophyllite join as determined from Rietveld refinements of X-ray powder data and for natural biotite G-117

	A44	a44n	sd12no.10	sd25no.10	sd37no.10	sd50no.10	sd62no.10	sd75no.10	sd87no.10	G-117
T-O1	1.620(12)	1.626(12)	1.637(10)	1.631(9)	1.627(9)	1.635(10)	1.630(6)	1.642(9)	1.644(10)	1.665(2)
T-O1	1.653(12)	1.654(12)	1.648(10)	1.664(9)	1.665(8)	1.673(10)	1.672(6)	1.671(8)	1.672(9)	1.669(2)
T-O2	1.665(7)	1.655(7)	1.652(6)	1.657(5)	1.665(5)	1.663(6)	1.667(6)	1.656(5)	1.665(6)	1.665(1)
T-O3	1.714(6)	1.713(6)	1.710(6)	1.604(5)	1.695(6)	1.705(7)	1.702(7)	1.697(9)	1.705(7)	1.680(2)
<T-O>	1.663	1.662	1.662	1.662	1.663	1.669	1.668	1.667	1.672	1.670
α*	3.57	3.50	1.35	5.50	7.57	9.63	10.33	11.55	12.12	7.97
M1-O3 ×4	2.120(9)	2.122(9)	2.109(6)	2.115(7)	2.117(7)	2.122(9)	2.118(8)	2.120(7)	2.114(8)	2.113(2)
M1-O4 ×2	2.103(15)	2.100(15)	2.113(10)	2.115(10)	2.092(11)	2.086(12)	2.091(10)	2.085(11)	2.092(11)	2.097(3)
<M1-O>	2.114	2.115	2.110	2.125	2.109	2.109	2.109	2.108	2.107	2.108
M2-O3	2.108(10)	2.106(9)	2.111(9)	2.098(7)	2.094(7)	2.079(8)	2.083(8)	2.069(8)	2.065(8)	2.092(2)
M2-O3	2.069(12)	2.076(12)	2.069(10)	2.068(8)	2.065(8)	2.061(8)	2.045(9)	2.045(8)	2.037(8)	2.086(2)
M2-O4	2.161(9)	2.158(9)	2.139(8)	2.141(7)	2.122(7)	2.119(7)	2.103(10)	2.102(6)	2.092(7)	2.076(2)
<M2-O>	2.113	2.113	2.106	2.103	2.094	2.086	2.077	2.072	2.065	2.085
t_{oct}†	2.211	2.213	2.214	2.198	2.179	2.152	2.141	2.215	2.126	2.160
$\psi M1$‡	58.44	58.54	58.54	58.76	58.97	59.33	59.50	59.90	59.77	59.18
$\psi M2$	58.42	58.49	58.46	58.56	58.73	58.96	58.97	59.21	59.09	58.80
K-O1 [i] ×4	3.181(12)	3.177(12)	3.207(7)	3.121(9)	3.076(9)	3.034(7)	3.016(12)	2.978(12)	2.964(9)	3.011(2)
K-O2 [i] ×2	3.144(9)	3.145(12)	3.140(8)	3.094(8)	3.060(7)	3.039(14)	2.999(14)	2.973(14)	2.953(9)	3.007(3)
K-O1 [o] ×4	3.319(8)	3.316(8)	3.291(7)	3.337(6)	3.382(6)	3.432(7)	3.451(5)	3.473(6)	3.483(6)	3.369(3)
K-O2 [o] ×2	3.243(9)	3.259(9)	3.250(8)	3.307(7)	3.332(7)	3.370(9)	3.426(9)	3.445(9)	3.474(8)	3.388(3)

* α = tetrahedral rotation angle; $\tan\alpha = \dfrac{2b(0.25 - y_{O1})}{0.5a}$ formula according to Hazen and Burnham (1973);

† t_{oct} octahedral sheet tickness; $t_{oct} = 2\left(0.5 - \dfrac{2(z_{O3} + z_{OH})}{3}\right)c_0 \sin\beta$ (Hazen and Burnham 1973);

‡ ψ = octahedral flattening angle; $\cos\Psi = \dfrac{t_{oct}}{2d_0}$ d_0 = mean cation to anion octahedral bond distance (Hazen and Burnham 1973).

Bond lengths. Data for the M2-O polyhedra (Fig. 4) show a distinct decrease as a function of trivalent cations (Al^{3+}_{tot} + [Fe^{3+}]), whereas on M1, there are only slight changes. This different behavior, which is most evident from Figure 4c confirms the results from those refinements, that Al^{3+} is predominately incorporated into the M2 site (Fig. 4d). Compared to single-crystal data of annite (Hazen and Burnham 1973), M1-O4 distances, found in this study, are slightly shorter, whereas M2-O4 distances are longer, all other M-O distances do agree rather well with single-crystal data (Hazen and Burnham 1973; G-117 biotite, Table 5). The octahedral flattening angle Ψ (Hazen and Burnham 1973) is 58.5(1)° in annite and the same for M1 and for M2. It significantly deviates from the ideal value of 54.73(8)° in a regular octahedron, and shows the annite octahedra to be flattened. With increasing sid-component, Ψ also increases, corresponding to the M1 site being more flattened (distorted) than the M2 site. The octahedral sheet thickness decreases from 2.21 Å in annite to 2.12 Å in micas richest in sid-components.

The variations of mean and individual T-O bond lengths with chemical composition are not very pronounced. According to the regression formula for <T-O> given by Hazen and

Burnham (1973) <T-O> should be 1.649 Å in annite and 1.689 Å in siderophyllite. Compared to single crystal data (Hazen and Burnham 1973; biotite G-117, Table 5), the T-O2 is systematically longer, whereas one of the two T-O1 interatomic distances is systematically shorter. O_{apical}-T-O_{basal} angles for the synthetic samples range between 106.5° and 110.8° in annite and 107.0–109.6° in the sid-rich samples, corresponding to slightly distorted tetrahedra. Single-crystal data, however, show the tetrahedra to be very regular with O_{apical}-T-O_{basal} angles between 110.2–110.4° in annite (Hazen and Burnham 1973) and

TABLE 6. Site occupation factors (normalized to a.p.f.u.) for synthetic micas on the ann-sid binary

Sample	{K+}	M1[Fe]	M1[Al³⁺]	M2[Fe]	M2[Al³⁺]
A44	0.956(8)	0.948(8)	–	1.97(1)	–
sd12no.10	0.99(1)	0.952(8)	0.048(2)	1.916(8)	0.072(8)
sd25no.10	0.992(4)	0.904(8)	0.096(8)	1.824(4)	0.156(8)
sd37no.10	0.964(8)	0.900(8)	0.100(8)	1.780(4)	0.228(8)
sd50no.10	0.936(8)	0.864(8)	0.136(12)	1.704(12)	0.368(12)
sd62no.10	0.940(12)	0.878(8)	0.122(12)	1.550(8)	0.462(12)
sd75no.10	0.928(4)	0.864(8)	0.136(8)	1.488(8)	0.612(8)
sd87no.10	0.920(4)	0.868(12)	0.132(12)	1.444(8)	0.668(8)

Note: Determined from Rietveld refinements of X-ray powder diffraction data.
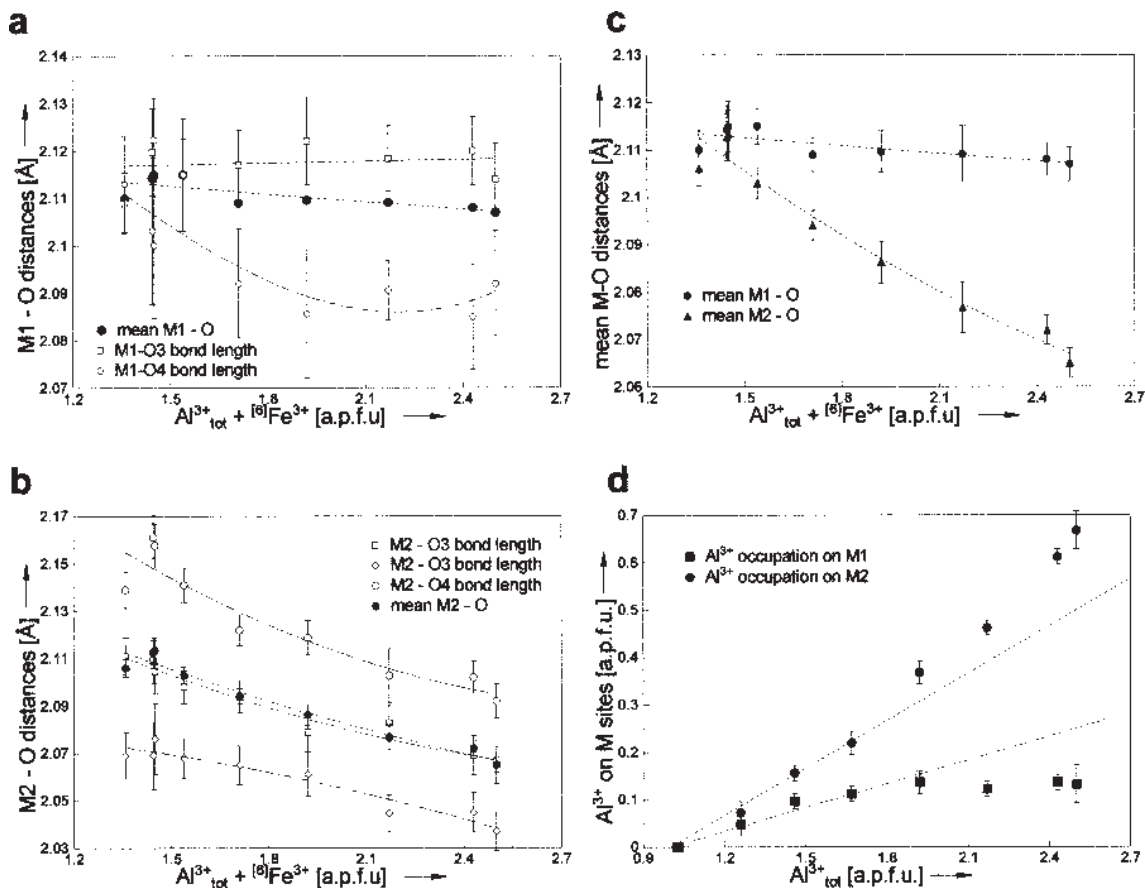

FIGURE 4. Variation of individual and mean octahedral M-O bond lengths of synthetic micas on the ann-sid binary, as determined from Rietveld refinement (**a–c**), and refined Al^{3+} occupancies on the octahedral M1 and M2 sites (**d**). Lines fitted to the data in Figure 4 a–c are guides to the eye, the dotted lines in Figure 4d corresponds to an equal distribution of Al^{3+} on M1 and M2.

between 109.8–110.0° for the Fe-Al rich biotite (G-117). The tetrahedra become more and more rotated with increasing Al^{3+} incorporation into annite. This is expressed by the increasing tetrahedral rotation angle α (Donnay et al. 1964) from ~1.0° in ann to 14.0° in the very aluminous biotites, see Figure 5.

Increasing tetrahedral rotation, there are pronounced changes in K-O interatomic distances. In the very aluminous annites, the inner K-O distances successively approach the lower limit of stability of the K-O bond lengths in these micas. From the *International Tables for Crystallography* (Wilson 1992), mean values for K-O distances in inorganic compounds and sixfold- to 12-fold-coordination are 2.83 Å to 3.07 Å.

Mössbauer spectroscopy

All single phase products were investigated by Mössbauer spectroscopy and nearly all annite spectra of Redhammer et al. (1993) were reinvestigated in terms of QSD analysis of thickness corrected spectra. The spectra were fitted with a n_1-n_2-n_3 model, where n_1, n_2, and n_3 are the numbers of assumed Gaussian components for $<Fe^{3+}>$, $[Fe^{3+}]$, and $[Fe^{2+}]$ respectively (cf. Rancourt et al. 1996). In all cases, n_1 is zero or one, n_2 is zero or one and n_3 is three (Table 7).

The spectra of annite (Figs. 6a–b) are described by two slightly asymmetrically broadened resonance absorption peaks, corresponding to $[Fe^{2+}]$ and small amounts of octahedrally and tetrahedrally coordinated ferric iron. The ferrous quadrupole splitting distribution exhibits a bimodal shape with overlapping Gaussian components centered at ~2.60 ($[Fe^{2+}]$-1) mm/s and ~2.30–2.45 mm/s($[Fe^{2+}]$–2). As noted by Redhammer (1998) for raw (i.e., not thickness corrected) spectra, end-member annite, synthesized at temperatures $T < 600$ °C exhibits a slightly different behavior as compared to samples synthesized at $T > 600$ °C. The "low temperature" annites do not show $<Fe^{3+}>$ contents but higher

[Fe³⁺] concentrations, which do not go beyond 10% of total iron. In these annites, $[Fe^{2+}]$-2 is centered rather constantly at 2.30 mm/s, the third Gaussian $[Fe^{2+}]$ component is centered around 2.30–2.40 mm/s ($[Fe^{2+}]$–3) and exhibits a very broad character. In the raw-spectra (Redhammer 1998), this component was centered at much lower quadrupole splittings and very low in intensity. "High" temperature annites show significant amounts of $<Fe^{3+}>$ but low $[Fe^{3+}]$ concentrations. For these annites the Gaussian component $[Fe^{2+}]$-2 is centered at larger splittings, $[Fe^{2+}]$–3 at lower splittings and both components show a decrease in quadrupole splitting with increasing ferric iron concentrations.

As siderophyllite content increases, the spectra become more asymmetrically broadened at the low velocity parts of the absorption lines (Figs. 6c–e). The spectra do not show evidence for $<Fe^{3+}>$ and the concentration of $[Fe^{3+}]$ decreases drastically. The $[Fe^{3+}]$ contents are below 1.5 % of total iron for samples with $x_{[Al]} > 0.37$. The ferrous QSD of the Al-rich samples is characterized by an intense peak at ~2.55 mm/s and a broad component centered at low quadrupole splittings, the shoulder centered at ~2.3 mm/s in the annite QSD progressively disappears. The splitting with highest probability, QS_{peak} ($[Fe^{2+}]$–1), decreases as well as the average splitting $<QS>$ (Figs. 7a and 7b). Furthermore, the Gaussian component positions of $[Fe^{2+}]$–2 and $[Fe^{2+}]$–3 also decrease as one moves from ann toward siderophyllic compositions. The "high"-temperature annites follow the trends, set up by the micas along the ann-sid binary, whereas the "low"-temperature annites do not show a significant dependence on the concentration of trivalent cations.

Infrared spectroscopy

The 4000–3000 cm^{-1} region. IR spectra of Redhammer et al. (1993) were reinvestigated with spectral fitting procedures. The spectra of annites with low $[Fe^{3+}]$ concentrations (Fig. 8a) are dominated by one prominent band centered around 3665 cm^{-1} and one broad band centered around 3530 cm^{-1}. A broad band centered at 3440 cm^{-1} is caused by adsorbed water. In addition, several shoulders are present. With increasing Fe^{3+} contents in annite, the broad 3530 cm^{-1} band becomes more pronounced and is dominating at very high Fe^{3+} concentrations (>30% of total iron, Fig. 8b). Mathematical decomposition yields up to 7 bands in the 3700–3500 cm^{-1} region. Unless the sometimes high amount of adsorbed water affects the superimposed hydroxyl bonds, positions for the different OH-cation configurations are constant within two wavenumbers for all annites having similar $[Fe^{3+}]$ concentrations. Independently of the choice of the set of starting parameters, final band positions were practically identical for a given sample. However, final band intensities showed a slight tendency of being dependent on the set of starting parameters. Thus no detailed discussion of band intensities will be given here. The results of spectral decomposition and band assignments are in Table 8.

According to Vedder (1964) the OH stretching bands can be classified into three main types. This nomenclature is used in this paper: N-bands (normal) are caused by OH groups, bonded to three divalent octahedral cations, I-bands (impurity), are caused by OH-groups, bonded to two divalent and one trivalent cation and finally V-bands (vacancy) are caused by OH-groups adjacent to a vacancy (Vedder 1964; Robert and Kodama
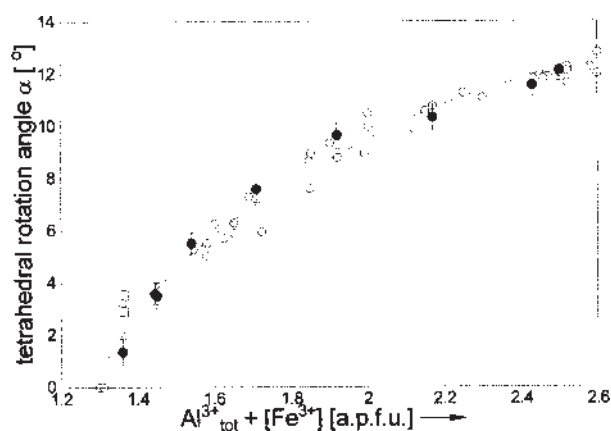

FIGURE 5. Variation of the tetrahedral rotation angle α of synthetic micas on the ann-sid binary. Filled circles are data calculated from refined fractional atomic coordinated according to the formula given by Hazen and Burnham (1973), open circles are data calculated according to the formula of Donnay et al. (1964) using b cell edge length. A guide to the eye was fitted to data, calculated according to Donnay et al. (1964).

TABLE 7. Mössbauer fit-parameter for thickness corrected folded 298K spectra of synthetic micas on the annite-siderophyllite binary*

Sample	$X_{[Al^{3+}]}$ a.p.f.u.	Site	δ_o mm/s	δ_1	Δ mm/s	$\sigma\Delta$ mm/s	Area %	χ^2_{red}
Ann no. 12	0.00	$[Fe^{2+}]$–1	1.102(2)	–0.0207	2.591(3)	0.13(2)	52.5	
		$[Fe^{2+}]$–2			2.31(1)	0.18(2)	23.8	
		$[Fe^{2+}]$–3			2.354(6)	0.60(9)	14.4	
		$[Fe^{3+}]$	0.320(3)	0	0.891(5)	0.42(4)	9.3(5)	1.10
Ann no.09	0.00	$[Fe^{2+}]$–1	1.104(2)	–0.0211	2.582(3)	0.13(2)	55.7	
		$[Fe^{2+}]$–2			2.30(2)	0.19(2)	23.0	
		$[Fe^{2+}]$–3			2.339(8)	0.59(8)	12.5	
		$[Fe^{3+}]$	0.315(3)	0	0.903(4)	0.41(4)	8.8(5)	1.30
Ann no.24	0.00	$[Fe^{2+}]$–1	1.159	–0.0120	2.602(3	0.11(2)	54.2	
		$[Fe^{2+}]$–2			2.33(1)	0.18(1)	27.2	
		$[Fe^{2+}]$–3			2.27(1)	0.68(9)	7.7	
		$[Fe^{3+}]$	0.350(4)	0	0.860(6)	0.44(5)	10.9(6)	1.155
Ann no.28	0.00	$[Fe^{2+}]$–1	1.139(2)	0.0030	2.589(4)	0.12(4)	42.3	
		$[Fe^{2+}]$–2			2.32(3)	0.20(2)	25.8	
		$[Fe^{2+}]$–3			2.22(1)	0.68(2)	9.6	
		$[Fe^{3+}]$	0.362(2)	0	0.80(1)	0.48(2)	22.3(6)	1.159
Ann no.44	0.00	$[Fe^{2+}]$–1	1.167(1)	–0.0050	2.596(2)	0.12(2)	49.6	
		$[Fe^{2+}]$–2			2.33(1)	0.20(7)	28.2	
		$[Fe^{2+}]$–3			1.79(4)	0.57(2)	8.6	
		$[Fe^{3+}]$	0.427(3)	0	1.012(7)	0.41(2)	10.4(5)	
		$(Fe^{3+}($	0.179(2)	0	0.355(6)	0.09(3)	3.2(2)	1.172
Ann no.66	0.00	$[Fe^{2+}]$–1	1.204(2)	–0.0273	2.596(8)	0.10(2)	41.9	
		$[Fe^{2+}]$–2			2.38(1)	0.19(4)	33.2	
		$[Fe^{2+}]$–3			2.185(6)	0.62(7)	17.9	
		$<Fe^{3+}>$	0.231(8)	0	0.403(2)	0.10(3)	7.0(8)	1.327
Sid12 no.10	0.11	$[Fe^{2+}]$–1	1.114(3)	0.0038(5)	2.626(2)	0.12(3)	44.4	
		$[Fe^{2+}]$–2			2.39(2)	0.23(1)	36.9	
		$[Fe^{2+}]$–3			2.26(1)	0.75(9)	16.0	
		$[Fe^{3+}]$	0.59(2)	0	0.79(2)	0.51(3)	2.7(8)	1.155
Sid25 no.10	0.26	$[Fe^{2+}]$–1	1.127(3)	–0.0015	2.618(3)	0.12(4)	42.9	
		$[Fe^{2+}]$–2			2.40(3)	0.19(1)	35.0	
		$[Fe^{2+}]$–3			2.26(1)	0.52(9)	19.3	
		$[Fe^{3+}]$	0.446(9)	0	0.84(2)	0.44(3)	2.8(6)	1.129
Sid37 no.10	0.33	$[Fe^{2+}]$–1	1.125(3)	–0.0011	2.595(7)	0.14(2)	50.4	
		$[Fe^{2+}]$–2			2.379(8)	0.25(3)	36.2	
		$[Fe^{2+}]$–3			2.15(1)	0.62(8)	11.8	
		$[Fe^{3+}]$	0.37(1)	0	1.01(2)	0.44(2)	1.6(6)	0.944
Sid50 no.10	0.51	$[Fe^{2+}]$–1	1.110(7)	0.0045	2.598(7)	0.14(1)	53.1	
		$[Fe^{2+}]$–2			2.34(1)	0.20(2)	25.2(7)	
		$[Fe^{2+}]$–3			2.24(2)	0.58(3)	21.7(2)	1.229
Sid62 no.2	0.67	$[Fe^{2+}]$–1	1.103(8)	0.0158	2.565(9)	0.14(2)	54.1	
		$[Fe^{2+}]$–2			2.28(1)	0.25(2)	17.3	
		$[Fe^{2+}]$–3			2.16(2)	0.69(9)	23.2	
		$[Fe^{3+}]$	0.38(1)	0	1.03(1)	0.54(6)	5.4(7)	1.019
Sid75 no.10	0.75	$[Fe^{2+}]$–1	1.094(11)	0.0102	2.560(9)	0.14(2)	59.9	
		$[Fe^{2+}]$–2			2.276(9)	0.14	10.1(7)	
		$[Fe^{2+}]$–3			2.18(2)	0.52(4)	30.0(4)	0.980
Sid87 no.2	0.84	$[Fe^{2+}]$–1	1.131(7)	0.0007	2.563(3)	0.15(1)	59.7	
		$[Fe^{2+}]$–2			2.29(1)	0.35(4)	18.9(9)	
		$[Fe^{2+}]$–3			2.12(1)	0.87(5)	21.4(3)	1.249
Sid100 no.2	0.78	$[Fe^{2+}]$–1	1.078(9)	0.0207	2.557(8)	0.13(2)	37.4	
		$[Fe^{2+}]$–2			2.28(1)	0.16(2)	8.5	
		$[Fe^{2+}]$–3			2.132(9)	0.63(2)	51.5	
		$[Fe^{3+}]$	0.55(6)	0	1.12(3)	0.50(5)	2.6(3)	1.007

* All fits impose $\Gamma=0.194$ mm/s and h-/h+ = 1; isomer shift δ is taken to be correlated to their quadrupole splitting Δ by $\delta = \delta_o + \delta_1 \Delta$.

1988). The dominating band at 3669 cm^{-1} is undoubtedly assigned to (OH) with (Fe^{2+}, Fe^{2+}, Fe^{2+}) as the octahedral cationic neighbors, N_D band (Boukili 1996; Robert and Kodama 1988 and references therein). Based on the evolution of IR spectra along the ann-sid join, the bands at 3650 cm^{-1} and 3628 cm^{-1} in annite are correlated with OH-[Fe^{2+}, Fe^{2+}, Al^{3+}] (I_B band) and OH-[Fe^{2+}, Fe^{2+}, Fe^{3+}] (I_A band) configurations, respectively. I-

bands have slightly increased FWHM of ~25 cm^{-1} as compared to the N_D band (~15 cm^{-1}). The broad V-type band, centered at 3530 cm^{-1}, is present in all annite spectra investigated here. It is assumed to be a superposition of two components associated with hydroxyl groups coordinated to [Fe^{2+}, Fe^{3+}, □] and [Fe^{3+}, Fe^{3+}, □] (V_A and V_C band, respectively). These two bands dominate the spectra of the Fe^{3+} rich annites, whereas V_A and V_A' are
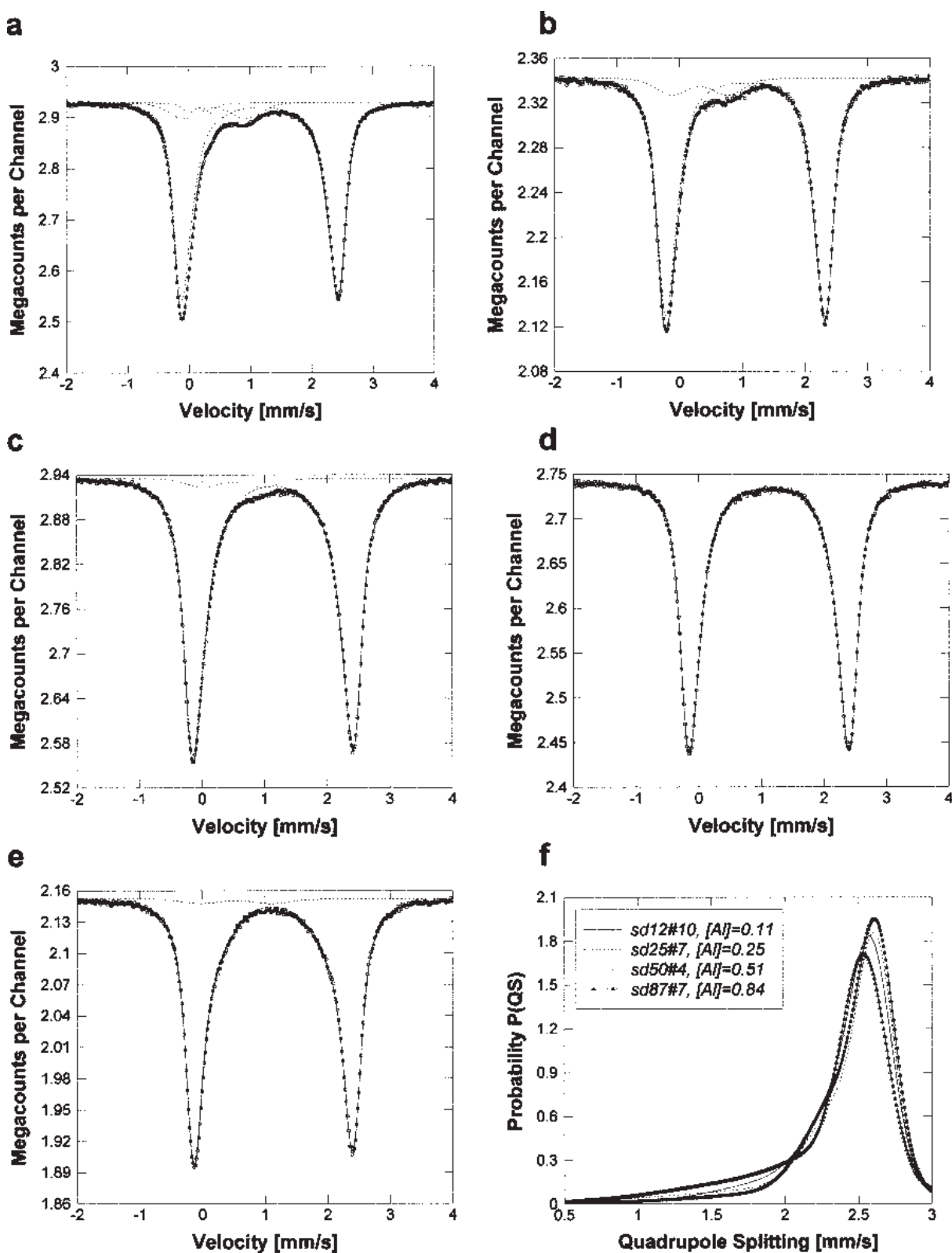
FIGURE 6. Refined thickness corrected Mössbauer spectra of selected micas on the ann-sid binary: (**a**) annite A44 with 10.4(4)% [Fe^{3+}] and 3.2(4)% <Fe^{3+}> of total iron, (**b**) annite A12 with 9.3(5)% [Fe^{3+}], (**c**) sid25 no. 2 with 4.0(4)% [Fe^{3+}], (**d**) sid50 no. 10, (**e**) sid100 no. 2 with 2.5(3)% [Fe^{3+}] and (**f**) representative quadrupole splitting distribution for Fe^{2+}.

low in intensity. Because of the somewhat higher band intensity in annites with low $[Fe^{3+}]/Fe_{tot}$ ratios, the band centered around 3590–3580 cm^{-1} is attributed to a $[Fe^{2+}, Al^{3+}, \square]$ configuration (V_A), and the remaining band to $[Fe^{3+}, Al^{3+}, \square]$ (V_A'). V-bands are generally broader than N-type and I-type bands.

Systematic behaviors appear along the ann-sid join (Figs. 8c–f). With increasing siderophyllite component the relative intensity of the band centered at ~3669 cm^{-1} in annite decreases, the one of the band centered at ~3656 cm^{-1} increases. The N_D and I_B bands are distinctly shifted toward lower wavenumbers with increasing Al_{tot}^{3+}. Similar behavior applies for increasing $[Fe^{3+}]$ contents in annite. Robert and Kodama (1988) report a similar behavior for the N, and I bands, whereas they observed an increase in band positions for the V-type bands in Mg-Al di- and trioctahedral micas. The vacancy bands of our samples are low in intensity, thus no clear systematics could be found. The band, centered around 3600 cm^{-1} in Al poor samples, gains intensity and is shifted toward 3610 cm^{-1} as a function of Al_{tot}^{3+} in micas richest in sid-component (see Table 8). Based on the band assignment for annite and on its presence in the Fe^{3+}-free samples, the band might be attributed to an OH-$[Fe^{2+}Al^{3+}\square]$ configuration (V_A band). Levillain and Maurel (1980) also observed a shoulder centered at ~3590 cm^{-1} in annite which evolves to ~3600 cm^{-1} with increasing sid-component, how-
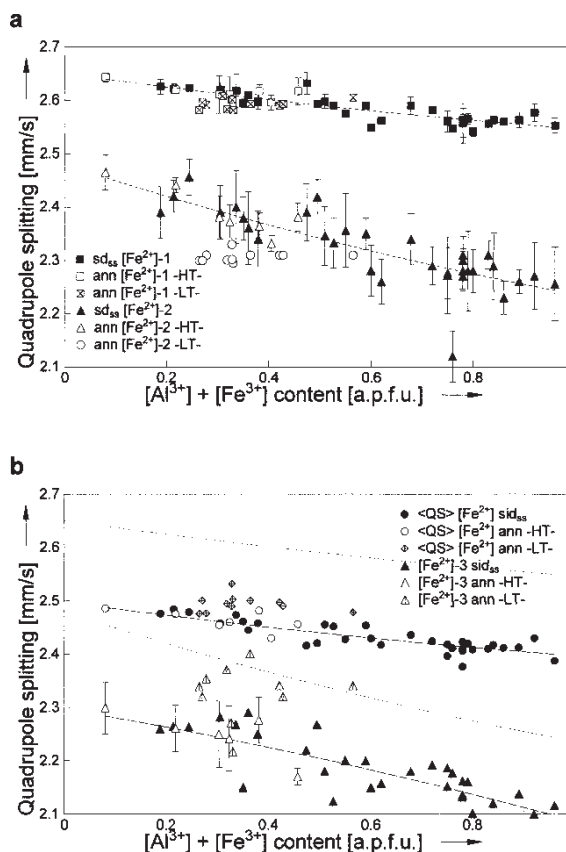

FIGURE 7. Variations of Mössbauer fit parameter of synthetic micas on the ann-sid binary as a function of octahedral trivalent cation content. Lines are guides to the eye to follow systematic trends. The data for $[Fe^{2+}]$-1 in (**a**) correspond to the quadrupole splitting with highest propability, QS_{peak}; <QS> in (**b**) corresponds to the mean quadrupole splitting of the ferrous quadrupole splitting distribution; the eye guides from (**a**) are included in (**b**).
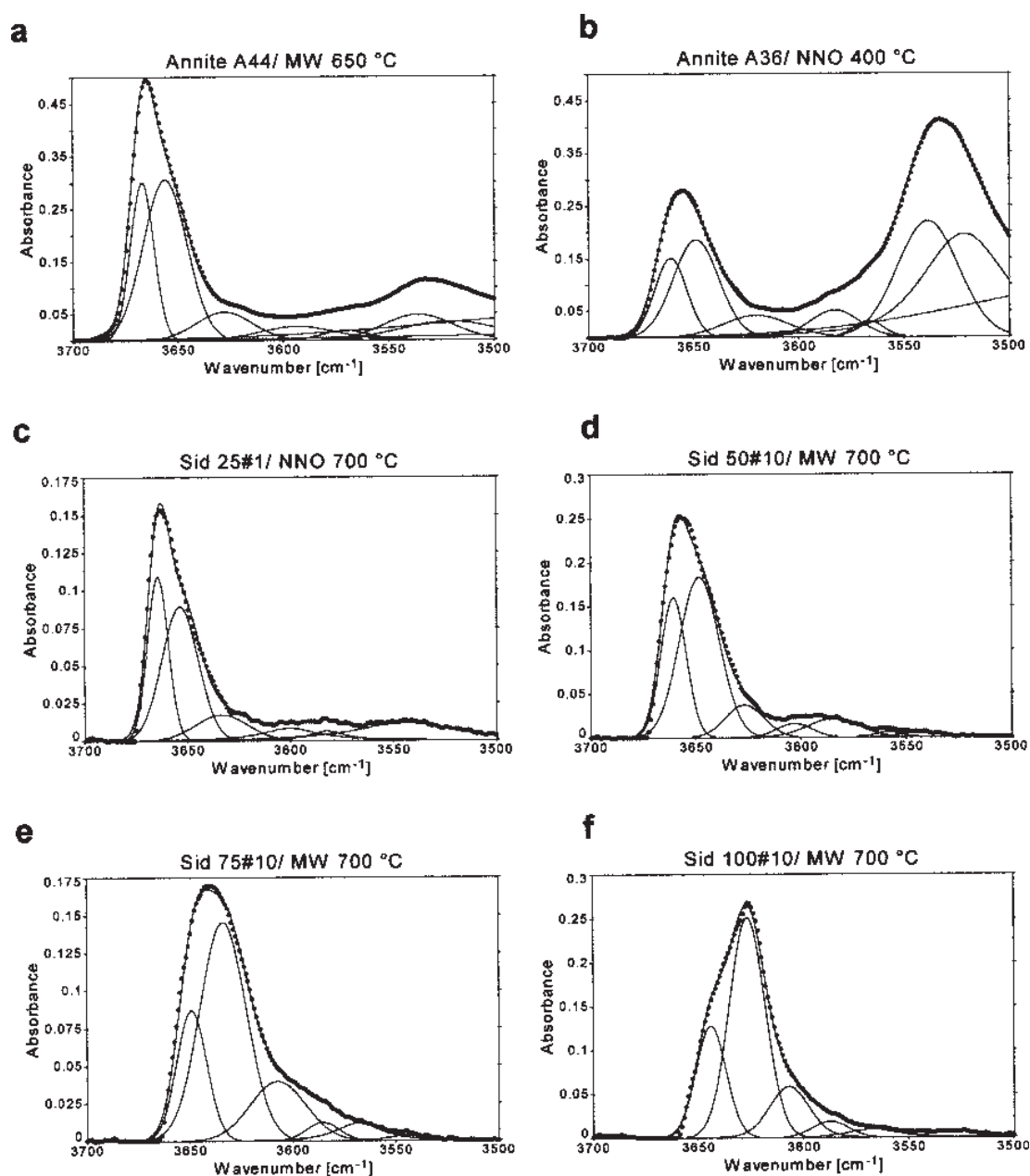
TABLE 8a. Results of spectral decomposition and band assignment of synthetic annite and ann-sid micas (units are cm^{-1}) — selected synthetic annites

A44	A20	A33	A36		Band assignment
3668	3669	3666	3661	N_D	OH - Fe^{2+}, Fe^{2+}, Fe^{2+}
3656	3656	3654	3649	I_B	OH - Fe^{2+}, Fe^{2+}, Al^{3+}
3628	3626	3626	3621	I_A	OH - Fe^{2+}, Fe^{2+}, Fe^{3+}
3593	3602	3584	3583	V_A	OH - Fe^{2+}, Al^{3+}, $\square$
3570	3573	3566	3566	V_A'	OH - Fe^{3+}, Al^{3+}, $\square$
3536	3543	3536	3539	V_B	OH - Fe^{2+}, Fe^{3+}, $\square$
3525	3527	3517	3521	V_C	OH - Fe^{3+}, Fe^{3+}, $\square$

TABLE 8b. Results of spectral decomposition and band assignment of synthetic annite and ann - sid micas (units are cm^{-1}) — Micas on the ann-sid join

sd12 no. 10	sd25 no. 10	sd37 no. 10	sd50 no. 1	sd50 no. 10	sd62 no. 10	sd75 no. 10	sd87 no. 10	sd100 no. 10	Band assignment
3667	3665	3663	3655	3661	3654	3650	3650	3644	N_D - OH - Fe^{2+}, Fe^{2+}, Fe^{2+}
3655	3654	3651	3645	3648	3640	3634	3630	3627	I_B - OH - Fe^{2+}, Fe^{2+}, Al^{3+}
3625	3629	3624	3626	3628	—	—	—	—	I_A - OH - Fe^{2+}, Fe^{2+}, Fe^{3+}
3600*	3601	3601	3600	3604	3610	3608	3609	3611	V_A - OH - Fe^{2+}, Al^{3+}, $\square$ /or: - OH - $2Al^{3+}$ Fe^{2+}
3582*	3582	3581*	3583	3585*	3685*	3586	3590	3587*	V_A' - OH - Fe^{3+}, Al^{3+}, $\square$
3547	3544	3543*	3541	3546*	3548*	—	—	—	V_B - OH - Fe^{2+}, Fe^{3+}, $\square$
3518*	3520*	—	3520*	—	—	—	—	—	V_C - OH - Fe^{3+}, Fe^{3+}, $\square$
1021	1033	1027	n.m.	1029	n.m.	1017	1014	1021	LO <Si-O> in plane
992	993	993	n.m.	996	n.m.	997	997	998	<Si-O> in plane
959	961	963	n.m.	966	n.m.	970	970	970	<Si-O> in plane
870	875	867	n.m.	878	n.m.	890	887	887	<Al-O>
768	767	767	n.m.	772	n.m.	784	784	787	<Si-O-Si>
706	707	710	n.m.	713*	n.m.	—	—	—	<Si-O-Si>
672	682	688	n.m.	688	n.m.	692	693	694	<Si-O-Al>
631	640	638	n.m.	640	n.m.	640	640	693	<Si-O-Al>
571	568	573	n.m.	582	n.m.	548	550	556	<Al-O>
—	499	509	n.m.	510	n.m.	531	533	531	[Al-O]
481.5	477	478	n.m.	492	n.m.	509	509	508	<Si-O>
459.0	451	456	n.m.	465	n.m.	477	477	479	<Si-O>

Note: n.m. = not measured.
* = very weak band.

FIGURE 8. FTIR spectra for synthetic micas $K[Fe_{3-x}Al_x]<Al_{1+x}Si_{3-x}>O_{10}(OH)_2$ on the ann-sid binary in the hydroxyl stretching region (**a**) synthetic annite, $[Fe^{3+}]$ concentration = 15% of total iron, (**b**) synthetic annite, $[Fe^{3+}]$ = 31% of total iron, (**c**) sid 25no. 1 with $x[Al^{3+}]$ = 0.26 apfu, $[Fe^{3+}]$ = 2.8% of total iron, (**d**) sid 50 no. 10 with $x[Al^{3+}]$ = 0.51 apfu, (**e**) sid 75 no. 10 with $x[Al^{3+}]$ = 0.75 apfu, (**f**) sid 100 no. 10 with $x[Al^{3+}]$ = 0.82 apfu.

ever, they attributed this band to an $OH-[Fe^{2+}Al^{3+}Al^{3+}]$ configuration. As we observed ordering of Al^{3+} onto the M2 site along the ann-sid join, $OH-[Fe^{2+}Al^{3+}Al^{3+}]$ configurations do exist and thus we tend to assign the band to an $OH-[Fe^{2+}Al^{3+}Al^{3+}]$ configuration. The positive correlation of band intensity with Al^{3+}_{tot} content supports this assignment.

The 1200–400 cm^{-1} region. In the lattice vibration range, samples were too dense for the 1000 cm^{-1} peaks (Fig. 9a) and

relative intensity is incorrect, however the density was necessary to resolve the weak peaks. All the bands in this region were assigned empirically by comparison of the spectra with different Al/Si ratios and by analogy with data of phlogopite, after Jenkins (1989). All spectra show two main absorption regions, centered around 1000 cm^{-1} and 450 cm^{-1}. Whereas the former is caused by stretching vibrations of the tetrahedral sheet, the latter also contains vibrations of the octahedral sheet, su-

perimposing bending vibrations of the tetrahedral sheet.

The dominating bands in the spectra at 998–992 cm^{-1} and 970–959 cm^{-1} are assigned to antisymmetric Si-O$_{br}$-Si stretching vibration (O$_{br}$ are the bridging O1 and O2 atoms), the low intensity shoulder at 1030–1017 cm^{-1} might be almost probably the longitudinal optic (LO) component of the strong 998–992 cm^{-1} peak. A weak shoulder in the spectra of the Al^{3+}-poor micas at 870 cm^{-1} evolves to a broad band with increasing Al^{3+} content. This band is assigned to Al-O vibrations. Jenkins (1989) found a strong shoulder at 915 cm^{-1} in phlogopite and assigned it to an in-plane Si-O-Al stretching vibration. The 768 cm^{-1} band is attributed to a tilting motion of the base of the SiO$_4$ tetrahedron and involves both stretching and bending motions. A band at 760 cm^{-1} in phlogopite was assigned by Jenkins (1989) to an Al-O stretching vibration, however, Papin et al. (1997) pointed out that a similar band is found at 777 cm^{-1} in Al-free tetrasilic Mg-mica, thus this band cannot be assigned to an Al-O vibration. The band at 706 cm^{-1} in the Al^{3+}-poor micas decreases in intensity with increasing Al^{3+} content, whereas the very weak bands at 672 and 631 cm^{-1} evolve to a clearly resolved, sharp doublet. As a consequence, the band firstly mentioned is assigned to Si-O-Si vibrations, the latter two to Si-O-Al vibrations. The band at 571–548 cm^{-1} might be assigned to a bending motion of Al-O but is more likely the LO component of the strong peak near 530 cm^{-1} ([Al-O]). In the broad absorption region centered around 450 cm^{-1}, several bands overlap, which are generated by [M]-O stretching motions in the octahedra and by Si-O bending vibrations (bands at 482 cm^{-1} and 459 cm^{-1} in the Al^{3+}-poor micas). A very weak band at ∼500 cm^{-1} in the Al^{3+} poor samples evolves to a pronounced peak at 530 cm^{-1} in the Al^{3+}-rich samples. This band is assigned to n[Al^{3+}-O]. For comparison, n[Mg-O] is found at 495 cm^{-1} in phlogopite (Jenkins 1989). Peaks below 450 cm^{-1} are not reliable because of poor detector resolution.

DISCUSSION

The octahedral sheet

The octahedral sheet exhibits the most pronounced reaction to the Tschermak's substitution. The lateral dimension within the (001) plane is decreased, as well as the octahedral sheet thickness t$_{oct}$. In general, the M1 site was found to be larger than the M2 site. These findings agree with the data of Hazen and Burnham (1973) for annite and the data obtained for Fe-Al rich biotite (G-117, Table 5). The slight decrease of the M1-O bond lengths indicates that this site accommodates only minor amounts of [Al^{3+}]. In contrast, the decrease of the bond lengths around the M2 sites correlates with the substitution of [Fe^{2+}] by [Al^{3+}]. For the first time, it was possible to detect a significant cationic preference of Al^{3+} for the M2 site along the ann-sid join. This is expressed by the occupation factors of Fe^{2+} and Al^{3+} on M1 and M2 as determined by the Rietveld refinements on the synthetic samples and by the very pronounced decrease of the mean <M2-O> distances. This behavior is not surprising as the larger cation [Fe^{2+}] tends to occupy the larger site, and [Al^{3+}] enters the smaller one (c.f. Weiss and Rieder 1985).

The octahedral flattening angles exhibit distinct distortions from ideal octahedral geometry. They show the M1 site to be more flattened, i.e., distorted, as compared to the M2 sites. The

octahedral flattening is positively correlated to the Al^{3+} content yielding larger deviations from ideal octahedral geometry in the aluminous micas as compared to annite.

Whereas X-ray diffraction gives us the mean structure of a compound, Mössbauer spectroscopy provides insight to the local structures around the Fe-probe nuclei. For the first time synthetic ann-sid micas were systematically investigated in terms of quadrupole splitting distribution analysis of thickness corrected spectra. The extracted QSDs are related to local environment populations around the Fe atoms, i.e., related to populations of crystallographic, chemical, geometric or electronic local distortion environments (LDEs of Rancourt et al. 1994b). However, without theoretical calculations linking LDEs to cor-
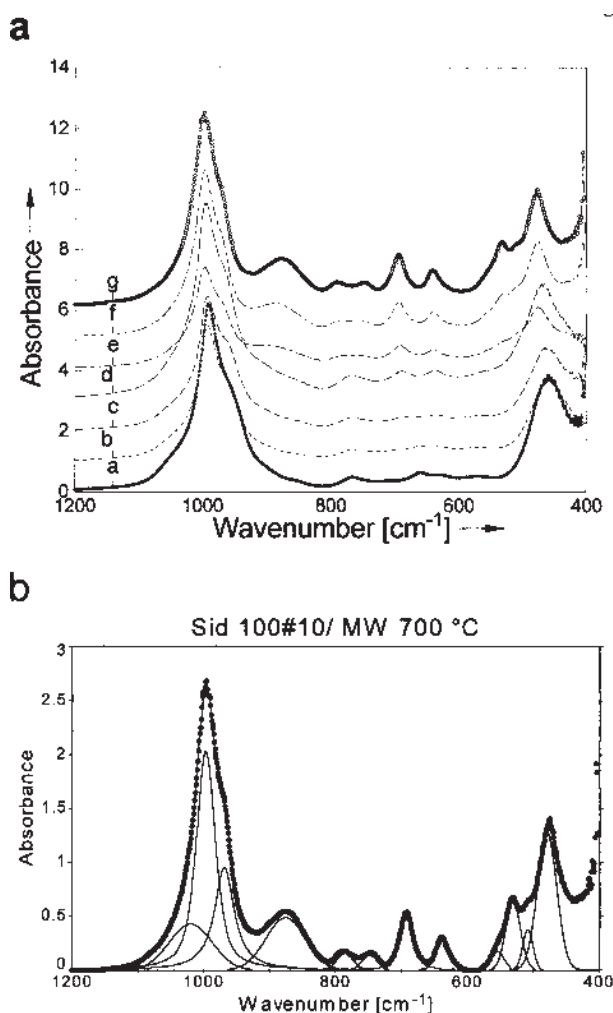

FIGURE 9. FTIR spectra for synthetic micas K[Fe$_{3-x}$Al$_x$]<Al$_{1+x}$Si$_{3-x}$>O$_{10}$(OH)$_2$ on the ann-sid binary in the 1200–400 cm^{-1} region. (**a**) a = sid12no. 10, x[Al^{3+}] = 0.11 apfu, b = sid25/no. 10, x[Al^{3+}] = 0.25 apfu, c = sid37no. 10, x[Al^{3+}] = 0.33 apfu, d = sid50/no. 10, x[Al^{3+}] = 0.51 apfu, e = sid75/no. 10, x[Al^{3+}] = 0.75 apfu, f = sid87/no. 10, x[Al^{3+}] = 0.78 apfu, g = sid100/no. 10, x[Al^{3+}] = 0.82 apfu; (**b**) decomposition of the FTIR spectrum of sample sid100/no. 10 into pseudo-Voigt components.

responding QSDs, we cannot give a detailed interpretation of the ferrous QSDs (Rancourt et al. 1994b, Redhammer 1998) but only can propose some explanations for the changes in appearance and shape of the QSDs along the ann-sid binary.

In the "low-temperature" annites, two discrete classes of LDEs are centered at 2.60 mm/s and 2.30 mm/s: one class which shows a large distribution of quadrupole splittings. The population of the latter group roughly correlates with the [Fe^{3+}] content. In "high-temperature" annites, which contain <Fe^{3+}> and—vice versa—[Al^{3+}] to compensate lateral geometric mismatch of octahedral and tetrahedral sheets (Redhammer 1998), the need for this third component is more evident. In these samples, it is centered at lower quadrupole splittings. Again, the population of this broad Gaussian component roughly correlates with the concentration of trivalent cations. In samples most enriched in [Al^{3+}], ~0.8 apfu [Fe^{2+}] populates this component, which is close to the octahedral aluminium content in these micas. This gives evidence for the presence of local structures, where [Fe^{2+}] tend to form clusters with 1:2 stoichiometry with trivalent cations, neighboring a central Fe^{2+} octahedron. These clusters were first proposed by Rancourt et al. (1994b) for annite and denoted as Fe^{2+} defect sites ([*Fe^{2+}]). In annite, these local structures might have a missing H atom for each trivalent cation to balance charge (Rancourt et al. 1994b). This must not necessarily hold true for the Al^{3+} enriched samples as they are balanced in charge. It is assumed, that Al^{3+} creates more distorted local structures around Fe^{2+} as does Fe^{3+}. The centers of the Gaussian component [Fe^{2+}]-3 are generally located at lower quadrupole splittings in [Al^{3+}] containing samples ("high-temperature" annites, ann-sid micas), as compared to the solely [Fe^{3+}] containing "low-temperature" annites. For intermediate to large overall geometric distortions of the Fe^{2+}-octahedra, as found in the micas, site distortion and quadrupole splitting are negatively correlated (cf. Redhammer 1998), which explains the slightly different behavior of the "low-temperature" annites.

In siderophyllite rich samples, the ferrous QSDs are dominated by a discrete group of LDEs centered around 2.55 mm/s and by the broad and distributed group of LDEs, which most probably are correlated with Fe^{2+} sites close to Al^{3+} octahedra. The shift of the QSD characteristics QS_{peak} and <QS> and of the centers of Gaussian components [Fe^{2+}]-2 and [Fe^{2+}]-3 toward lower quadrupole splittings with increasing [Al^{3+}] (trivalent cation) content points at increasing distortion from ideal octahedral geometry of all corresponding Fe^{2+} octahedra as siderophyllite content increases. The above findings agree with the increasing octahedral flattening angle y as one moves from ann-toward sid-rich compositions.

In general, the hydroxyl stretching frequencies (3800–3400 cm^{-1} region) of micas are affected by the octahedral cations, in close neighborhood to the hydroxyl group and by the configuration and charge distribution of the tetrahedral sheets, being in second nearest neighborhood. Robert and Kodama (1988) pointed out that any shift in the frequency of OH-bands reflects changes in the environment of the OH dipoles and in the O-H···O hydrogen bond distances.

For the micas investigated here, the N_D bands show the highest wavenumbers observed for a specific composition, thus in-

dicating the strongest O-H bond for these bands among all other bands. The progressive replacement of <Si^{4+}> by <Al^{3+}> along the ann-sid join creates local charge imbalances (residual charges) at the oxygen atoms of the tetrahedra. Rings of six tetrahedra may have the compositions Al_2Si_4 or even Al_3Si_3 for the high Al contents along the ann-sid join. Furthermore the tetrahedral rotation angle α increases from ~1–3° in annite to 12.2° in micas richest in sid component thus shortening the O-H···O_{tet} bonds. Both phenomena favor the enhancement of the O-H···O_{tet} bond (Robert and Kodama 1988), and thus weaken the O-H bond strength. This is experimentally observed by the shift of the N_D band toward lower wavenumbers.

The I bands ($2M^{2+}$, M^{3+}) show generally lower OH stretching wavenumbers, because of the higher valence sum, the OH oxygen atom (O4) receives from the three neighboring cations; i.e., 1.17 valence units for the I-type bands as compared to 1.0 valence units for N-type bands (Robert and Kodama 1988). Fe^{3+} introduces a larger shift than Al^{3+} owing to its larger electronegativity. The wavenumber decrease of the I_b band with increasing Al³⁺ for Si⁴⁺ substitution is caused by similar effects as for the N-type bands: increasing residual charges on the tetrahedra results in a tilting of the OH-vector, increasing α-rotation results in a shortening of the O-H···O_{tet} bonds, both leading to a weakening of the O-H bond strength.

The V-type bands have the OH vector tilted away from the **c*** direction because of the empty third octahedral cation site. Because of the tilting, the H^+ gets closer to two O3 oxygen atoms (apical oxygen) resulting in a stronger O-H···O_{tet} bond as compared to the N- and I-type bands (Robert and Kodama 1988). This weakens the O-H bond strength and results in V-type bands at low wavenumbers.

Tetrahedral sheet and interlayer

The tetrahedron is remarkably regular in the aluminous iron micas as indicated by the single crystal structure investigation of the Al-Fe rich biotite. It is assumed that this applies also to the synthetic micas on the ann-sid join, even if the Rietveld refinements suggested stronger distortions from ideal geometry. As Al^{3+} successively replaces Si^{4+} in the tetrahedra and Fe^{2+} in the octahedra, the octahedral sheet becomes smaller than the tetrahedral one, matching of the two sheets is achieved by flattening of the octahedra and by reducing the lateral dimension of the tetrahedral sheet through α-rotation (ditrigonal distortion). Thus we observe a positive correlation between the Al^{3+}_{tot} contents and the tetrahedral rotation angle. The maximum α-rotation itself is limited by the size of the interlayer cation, limiting in turn the Al^{3+} solubility in annite. The ditrigonal distortion of the in annite fully expanded hexagonal tetragonal rings ($\alpha = 0°$) has a direct influence on the coordination of the {K^+} cation. It changes from a regular 12-fold site for $\alpha = 0°$ to a regularly sixfold and sixfold-coordinated polyhedron if α approximates the theoretically maximum rotation angle of 30°. Hence, two of the four independent K-O distances are successively shortened. The maximum value of the tetrahedral rotation angle is set by the distance between the interlayer cation and the bridging oxygen atoms of the tetrahedra. For trioctahedral potassium micas, α-rotation angles larger than 14.5° were not observed (Robert 1981; Robert and Kodama 1988), assuming this value to be the upper possible tet-

rahedral rotation angle for these compounds. The largest value of this study is $\alpha = 14.0°$ for sid100/no. 5 with $x = 0.92$. For this compound, the two shortest K-O distances are distinctively shorter than 2.95 Å, which is very close to the lower limit for K-O interatomic distances. Preiswerkite $\{Na\}[Mg_2Al]<Si_2Al_2>O_{10}(OH)_2$ with the smaller $\{Na^+\}$ has a tetrahedral rotation angle of $\alpha = 20.0°$ (Oberti et al. 1993). As a consequence higher Al^{3+}_{tot} contents are possible in this mineral. In clintonite $\{Ca\}[Mg_2Al]<SiAl_3>O_{10}(OH)_2$, Ca^{2+} occupies the interlayer site, the tetrahedral rotation angle is $\alpha = 23.1°$ (Joswig et al. 1986) thus allowing the very high $<Al^{3+}>$ content of 2.69 apfu in the sample studied by the above authors. This all suggests, that the size of the interlayer cation controls and limits the possible amount of tetrahedral rotation and consequently the limits for Al^{3+} incorporation.

However, the "limiting" value of the tetrahedral rotation angle $\alpha = 14.5°$ does not correspond to the actual value of α at synthesis temperature. It is well known, that large polyhedra with high coordination number can expand much more than those with low coordination number. Takeda and Morosin (1975) found the thermal expansion of the tetrahedra in synthetic fluorphlogopite $\{K\}[Mg_3]<AlSi_3>O_{10}F_2$ to be negligible whereas the octahedra expand significantly. The mean Mg-O distances were 2.070 Å and 2.094 Å at room temperature and 700 °C respectively. However, the most expansible polyhedron is around the K-site. Mean K-O_{inner} interatomic distances increased from 2.987 Å to 3.116 Å in synthetic fluorphlogopite (Takeda and Morosin 1975). Hence at lower synthesis temperatures, the space needed by the K^+ cation in the structure, is lower than at higher temperatures. This leads to stronger ditrigonal distortion of the tetrahedral sheet and consequently allows higher Al^{3+} solubility in the lower-temperature synthesis runs (c.f. Fig. 2).

Fe²⁺ M2:M1 site occupation by Mössbauer spectroscopy

Rancourt (1994a, 1994b) and Rancourt et al. (1994b) have discussed that cis-M2 and trans-M1 sites in layer silicates cannot be resolved by Mössbauer spectroscopy. Here we provide further evidence for the impossibility of resolving M1 and M2 sites. Recalling the evolution of shape of the ferrous QSD, we find a progressive decrease of intensity of the QSD component $[Fe^{2+}]$-2. This made Levillain et al. (1981) to conclude the Mössbauer spectrum of siderophyllite to be composed of only one doublet. However their spectrum (Fig. 1 in Levillain et al. 1981) exhibits some residual absorption due to Fe^{2+} ($[Fe^{2+}]$-2). The $[Fe^{2+}]$-2 component was assigned to the trans-M1 site in literature (e.g., Redhammer et al. 1993). According to this assignment, a negative correlation between the amount of Fe^{2+} on the M1 site and the Al^{3+} content of the mica studied here, may be derived, thus yielding a strong preference of Al^{3+} for the M1 site. Levillain et al. (1981) also concluded, that Fe^{2+} only occupies the M2, Al^{3+} exclusively the M1 site in siderophyllite.

However, the present results from X-ray powder diffraction refinements on the samples studied by Mössbauer spectroscopy, do not support an ordering of Al^{3+} onto the M1 site. In contrast, we observe a preference of Al^{3+} for the M2 site which also is proven by single crystal structure refinements on the Fe-Al rich biotite G-117. Hence, if it were possible to ex-

tract reliable M2/M1 area ratios from the Mössbauer spectra of the micas, we should observe spectra with the components $[Fe^{2+}$-1] and $[Fe^{2+}$-2] becoming equal in intensity as the $[Al^{3+}]$ content increases. This is actually not the case, instead the opposite is found. Thus we conclude that, despite all other difficulties mentioned in the literature (Rancourt 1994a, 1994b; Rancourt et al. 1994b, and references therein), the ferrous QSD components $[Fe^{2+}1]$-1 and $[Fe^{2+}]$-2 do not correspond to a specific crystallographic site (M1 of M2), but arise from local geometric and/or electronic distortion environments around the Fe atoms within the octahedral sheet of the micas. This confirms the impossibility of extracting M2/M1 area ratios from Mössbauer spectroscopy.

Charge balance in annite

As found in previous studies (Redhammer et al. 1993; Mercier et al. 1996; Redhammer. 1998), annite shows a lower limit of Fe^{3+}/Fe_{tot} content to compensate the dimensional misfit between the large $Fe^{2+}O_6$ octahedral sheet and the smaller $AlSi_3$ tetrahedral sheet. V-bands are always present in IR spectra of annite. Vacancies are predominantly clustered around OH with two Fe^{3+} cations and with one Fe^{2+} and one Fe^{3+} cation (V_C and V_B band, respectively). Clusters with vacancies and $Fe^{2+/3+}$ and Al^{3+} atoms only play a minor role. As there is a positive correlation between total octahedral ferric iron content and the intensity of the V bands, we might conclude, that the creation of octahedral vacancies by the mechanism $3\ [Fe^{2+}] \rightarrow 2\ [Fe^{3+}] + [?]$ plays a major role in achieving bulk charge balance. This was pointed out by Redhammer et al. (1993) and independently confirmed by the work of Rebbert et al. (1995). Furthermore, Boukili (1996) demonstrated, that the V-band intensity of highly oxidized annite (e.g., synthesized at NNO solid state buffer conditions) decreases, if the annite is tempered in a hydrothermal experiment at more reducing conditions (e.g., MW conditions) leading to lower $[Fe^{3+}]$ contents. However dehydroxylation might also play a role in achieving bulk charge balance in the hydrothermal experiments. The strikingly positive correlation between V-band intensity and $[Fe^{3+}]$ content was predominantly found for pre-synthesized annites, tempered hydrothermally at different temperatures and redox conditions (cf. Redhammer et al. 1993).

REFERENCES CITED

Annersten, H. (1974) Mössbauer studies of natural biotites. American Mineralogist, 59, 143–151.

Benisek, A., Dachs, E., Redhammer, G., Tippelt, G., and Amthauer, G. (1996) Activity-composition relationship in Tschermak's substituted biotites at 700°C, 2 kbar. Contribution to Mineralogy and Petrology, 125, 85–99.

Benisek, A., Dachs, E., and Cemic, L. (1999) Heat capacities of Tschermak substituted Fe-biotites. Contribution to Mineralogy and Petrology, 135, 53–61.

Boukili, B. (1996) Cristallochimie des biotites ferro-alumineuses de synthèse dans le systemè Na$_2$O-K$_2$O-FeO-Fe$_2$O$_3$-Al$_2$O$_3$-SiO$_2$-H$_2$O-HF. Thesis, Université d'Orléans, 250 pp.

Brigatti, M.F. and Davoli, P. (1990) Crystal-structure refinements of 1M biotites. American Mineralogist, 75, 305–313.

Brigatti, M.F., Galli, E., and Poppi, L. (1991) Effect of Ti substitution in biotite-1M crystal chemisty. American Mineralogist, 76, 1174–1183.

Cagliotti, G., Paoletti, A., and Ricci, F.P. (1958) Choice of collimators for a crystal spectrometer for neutron diffraction. Nuclear Instruments, 3, 223–228.

Cyang, G.L., Chou, I.-M., and Sherman, D.M. (1996) Reinvestigation of the annite = sanidine + magnetite + H$_2$ reaction using the fH$_2$-sensor technique. American Mineralogist, 81, 475–484.

Dachs, E. (1994) Annite stability revised. 1. Hydrogen sensor data for the reaction annite = sanidine + magnetite + H$_2$. Contributions to Mineralogy and Petrology, 117, 229–240.

Della Ventura, G., Robert, J.-L., Raudsepp, M., and Hawthorne, F.C. (1993) Site occupancies in monoclinic amphiboles: Rietveld structure refinement of synthetic nickel magnesium cobalt potassium richterite. American Mineralogist, 78, 633–640.

Donnay, G., Donnay, J.D.H., and Takeda, H. (1964) Trioctahedral one layer micas. II. Prediction of the structure from composition and cell dimensions. Acta Crystallographica, 17, 1374–1381.

Dyar, M.D. (1990) Mössbauer spectra of biotites from metapelites. American Mineralogist, 75, 656–666.

Dyar, M.D. and Burns, R. (1986) Mössbauer spectral study of ferruginous one-layer trioctahedral micas. American Mineralogist, 71, 955–965.

Farmer, V.C. (1974) The layer silicates. In "The Infrared Spectra of Minerals", Ed.: V.C. Farmer, The Mineralogical Society of Great Britain, London. 331–363.

Hamilton, D.L. and Henderson, C.M.B. (1968) The preperation of silicate compositions by a gelling method. Mineralogical Magazine, 35, 832–838.

Hazen, R.M. and Burnham, C.W. (1973) The crystal structure of one-layer phlogopite and annite. American Mineralogist, 58, 889–900.

Hewitt, D.A. and Wones, D.R. (1975) Physical properies of som Fe-Mg-Al trioctahedral biotites. American Mineralogist, 60, 854–862.

Hill, R.J. and Fischer, R.X. (1990) Profile agreement indices in Rietveld and pattern fitting analysis. Journal of Applied Crystallography, 23, 462–468.

Jenkins, D.M. (1989) Empirical Study of the Infrared Lattice Vibrations (1100–350 cm^{-1}) of Phlogopite. Physics and Chemistry of Minerals, 16, 408–414.

Joswig, W., Amthauer, G., and Takeuchi, Y. (1986) Neutron-diffraction and Mössbauer spectroscopic study of clintonite (xanthophyllite). American Mineralogist, 71, 1194–1197.

Levillain, C. and Maurel, P. (1980) Etude par spectrometrie infrarouge des frequences d'elongation du groupement hydroxyle dans des micas synthetiques de la serie annite-phlogopite et annite-siderophyllite. C R Acad Sc Paris, t 290 (2 juin 1980), Serie D, 1289–1292.

Levillain, C., Maurel, P., and Menil, F. (1981) Mössbauer studies of synthetic and natural micas on the polylithionite-siderophyllite join. Physics and Chemistry of Minerals, 7, 71 –76.

Mercier, P.H.J., Rancourt, D.G., and Berman, R.G. (1996) Aspects of the crystal chemistry of annite mica. Italian Physical Society, Conference Proceedings Vol. 50, International Conference on the Application of the Mössbauer Effect, ICAME-95, Rimini, edited by I. Ortalli, 789–792.

Oberti, R., Ungaretti, L., Tlili, A., Smith, D.C., and Robert J.-L. (1990) The crystal structure of preiswerkite. American Mineralogist, 78, 1290–1298.

Papin, A., Sergent, J., and Robert, J.-L. (1997) Intersite OH-F distribution in an Al-rich synthetic phlogopite. European Journal of Mineralogy, 9, 501–508.

Ping, J.Y., Rancourt, D.G., and Stadnik, Z.M. (1991) Voigt-based methods for arbitrary-shape quadrupole splitting distributions (QSD´s) applied to quasi-crystals. Hyperfine Interactions, 69, 493–496.

Rancourt, D.G. (1994a) Mössbauer Spectroscopy of Minerals I. Inadequacy of Lorentzian-line doublets in fitting spectra arising from quadrupole splitting distributions. Physics and Chemistry of Minerals, 21, 244–249.

——— (1994b) Mössbauer Spectra of Minerals II. Problem of resolving cis and trans octahedral Fe^{2+} sites. Physics and Chemistry of Minerals, 21, 250–257.

Rancourt, D.G. and Ping, J.Y. (1991) Voigt-based methods for arbitrary-shape static hyperfine parameter distribution in Mössbauer spectroscopy. Nuclear Instruments and Methods in Physics Research, B58, 85–97.

Rancourt, D.G., Christie, I.A.D., Royer, M., Kodama, H., Robert, J.-L., Lalonde, A.E., and Murad, E. (1994b) Determination of accurate [4]Fe^{3+}, [6]Fe^{2+} and [6]Fe^{2+} site populations in synthetic annite by Mössbauer spectroscopy. American Mineralogist, 79, 51–62.

Rancourt, D.G., Ping, J.Y., and Berman, R.G. (1994a) Mössbauer spectroscopy of minerals III. Octahedral-site Fe^{2+} quadrupole splitting distributions in layer silicates. Physics and Chemistry of Minerals, 21, 258–267.

Rancourt, D.G., Ping, J.Y., Boukili, B., and Robert, J.-L. (1996) Octahedral-site Fe^{2+} quadrupole splitting distributions from Mössbauer spectroscopy along (OH, F)-annite join. Physics and Chemistry of Minerals, 23, 63–71.

Rebbert, C.R., Partin, E., and Hewitt, D.A. (1995) Synthetic biotite oxidation under hydrothermal conditions. American Mineralogist, 80, 345–354.

Redhammer, G.J. (1998) Mössbauer spectroscopy of synthetic trioctahedral micas. in: Rancourt, D.G. (ed.): Mössbauer spectroscopy in clay science. Hyperfine Interactions, 117, 85–115.

Redhammer, G.J., Beran, A., Dachs, E., and Amthauer, G. (1993) A Mössbauer and X-ray diffraction study of annites synthesized at different oxygen fugacities and crystal chemical implications. Physics and Chemistry of Minerals, 20(6), 382–394.

Redhammer, G.J., Dachs, E., and Amthauer, G. (1995) Mössbauer spectroscopic and X-ray powder diffraction studies of synthetic micas on the join Annite KFe$_3$AlSi$_3$O$_{10}$(OH)$_2$–Phlogopite KMg$_3$AlSi$_3$O$_{10}$(OH)$_2$. Physics and Chemistry of Minerals, 22, 282–294.

Rietveld, H.M. (1969) A profile refinement method for nuclear and magnetic structures. Journal of Applied Crystallography, 2, 65–71.

Robert, J.-L. (1981) Etudes cristallochimiques sur les micas et les amphiboles, applications a la petrographie et a la geochimie: These d' etat, Univ. Paris. XI, 205 pp.

Robert, J.-L. and Kodama, H. (1988) Generalization of the correlations between hydroxyl-stretching wavenumbers and composition of micas in the system K$_2$O-MgO-Al$_2$O$_3$-SiO$_2$-H$_2$O: a single model for trioctahedral and dioctahedral micas. American Journal of Science, 288-A, 196–212.

Rodriguez-Carvajal, J. (1996) FULLPROF: Rietveld, Profile Matching and Integrated Intensity Refinement of X-ray and Neutron Data (PC-version). Version 1.3c.

Rutherford, M.J. (1973) The phase relations of aluminous iron biotites in the system KAlSi$_3$O$_8$-KAlSiO$_4$-Al$_2$O$_3$-Fe-O-H. Journal of Petrology, 14, 159–180

Takeda, H. and Morosin, B. (1975) Comparison of observed and predicted structural parameters of mica at high temperature. Acta Crystallographica, B31, 2444–2452.

Vedder, W. (1964) Correlation between infrared spectrum and chemical composition of mica. American Mineralogist, 49, 736–788.

Weiss, Z. and Rieder, M. (1985) Geometry of the octahedral coordination in micas: a review of refined structures. American Mineralogist, 70, 747–757.

Wilson, A.J.C. Ed. (1992) International Tables for Crystallography, Vol. C, Mathematical, Physcial and Chemical Tables. Chapter 9.6, 707 ff. Kluwer, Dortrecht.